ABSTRACT

Title of dissertation: PARTICLE HEATING AND ENERGY PARTITION IN RECONNECTION WITH A GUIDE FIELD

Qile Zhang
Doctor of Philosophy, 2019

Dissertation directed by: Professor James Drake
Department of Physics

Kinetic Riemann simulations have been completed to explore particle heating during reconnection with a guide field in the low-beta environment of the inner heliosphere and the solar corona. The reconnection exhaust is bounded by two rotational discontinuities (RDs) with two slow shocks (SSs) that form within the exhaust as in magnetohydrodynamic (MHD) models. At the RDs, ions are accelerated by the magnetic field tension to drive the reconnection outflow as well as flows in the out-of-plane direction. The out-of-plane flows stream toward the midplane and meet to drive the SSs. The turbulence at the SSs is weak so the shocks are laminar and produce little dissipation, which differs greatly from the MHD treatment. Downstream of the SSs the counter-streaming ion beams lead to higher density and therefore to a positive potential between the SSs that confines the downstream electrons to maintain charge neutrality. The potential accelerates electrons from upstream of the SSs to downstream and traps a small fraction but only produces modest electron heating. In the low-beta limit the released magnetic energy is split between bulk flow and ion heating with little energy going to electrons.

To firmly establish the laminar nature of reconnection exhausts, we explore the role of instabilities and turbulence in the dynamics. Two-dimensional reconnection and Riemann simulations reveal that the exhaust develops large-amplitude striations resulting from electron-beam-driven ion cyclotron waves. The electron beams driving the instability are injected into the exhaust from one of the RDs. However, in 3D Riemann simulations, the additional dimension results in a strong Buneman instability at the RD, which suppresses electron beam formation. The 3D simulation does reveal a weak ion-ion streaming instability within the exhaust. All these instabilities become weaker with higher ion-to-electron mass ratio due to higher electron thermal speed. We also use a kinetic dispersion relation solver to show that the ion-ion instability will become stable in conditions expected under lower upstream beta. The results suggest that in realistic reconnection exhausts, which have three dimensions and real mass ratio, the kinetic-scale turbulence that develops will be too weak to play a significant role in energy conversion.

PARTICLE HEATING AND ENERGY PARTITION IN RECONNECTION WITH A GUIDE FIELD

by

Qile Zhang

Dissertation submitted to the Faculty of the Graduate School of the
University of Maryland, College Park in partial fulfillment
of the requirements for the degree of
Doctor of Philosophy
2019

Advisory Committee:
Professor James Drake, Chair/Advisor
Dr. Michael Swisdak, Co-Advisor
Professor Adil Hassam
Professor Thomas Antonsen
Professor Dennis Papadopoulos

Dedication

To my mom, and my fiancée.

Acknowledgments

I would like to first thank my advisor Jim Drake and co-advisor Marc Swisdak. It is my privilege to join such an amazing group and learn from extraordinary individuals like them. Discussing with them is always thought-provoking, inspiring and informative. Working on challenging research problems with them is a lifelong beneficial experience for me. I am grateful for their patient guidance and support over the years, especially during the hard times when I confronted difficulties in my research projects.

I would also like to thank other professors and scientists past and present in the plasma theory group: Tom Antonsen, Adil Hassam, Bill Dorland, Matt Landreman, Jason TenBarge, Ian Abel. As experts in the field, they contributed much wisdom and experience into our discussions in the group meetings and inspired me to explore different aspects of the world of plasma physics. I also want to thank other professors in UMD that have helped me in the journey of grad school, including Dennis Papadopoulos, Roald Sagdeev, Chuan Sheng Liu, etc. Special thanks go to Tom Antonsen, Adil Hassam, Dennis Papadopoulos for graciously agreeing to sit on my committee.

Thanks also go to other young colleagues past and present in the plasma theory group: Joel Dahlin, Wrick Sengupta, Lora Price, Gareth Roberg-Clark, Harry Arnold, Tak Chu Li, Jimmy Juno, Elizabeth Paul, Mike Martin, Rahul Gaur, George Wilkie, Anjor Kanekar, Obioma Ohia, Alessandro Geraldini, Rogrio Jorge, etc. They are so kind, smart, knowledgeable and embracing different cultures. I

learned a lot from them and we had a lot of fun together.

I also want to acknowledge the support from people in the scientific community outside UMD, including Mike Shay, Colby Haggerty, Paul Cassak, Yi-Hsin Liu, Haihong Che, Judy Karpen, Chuanfei Dong, Yimin Huang, Dana Longcope, etc. Besides, I appreciate Prof. Guang Chen and his family for giving me helpful advice on grad school and my career. I also appreciate my undergraduate advisor Prof. Shaojie Wang for encouraging me to come to UMD and study plasma physics.

I am also thankful to the past or present IREAP and physics department staffs who take care of my administrative procedures or technological needs. They include: Jane Hessing, Linda Ohara, Pauline Rirksopa, Paulina Alejandro, Roxanne Defendini, Mohini Kaul, Nancy Boone, Josiland Chambers, Ed Condon, etc.

Finally, I owe my deepest thanks to my mother and my fiancée. Their love, acceptance, companion and support give me strength to walk through this challenging but rewarding journey.

Table of Contents

List of Tables

List of Figures

List of Abbreviations

β	plasma beta (the ratio of thermal pressure to magnetic pressure)
MHD	Magnetohydrodynamics
TRACE	Transition Region and Coronal Explorer
RHESSI	Reuven Ramaty High Energy Solar Spectroscopic Imager
CME	Coronal Mass Ejection
PIC	particle-in-cell
CFL	Courant-Friedrichs-Lewy
RD	rotational discontinuity
SS	slow shock
PSP	Parker Solar Probe

Chapter 1: Introduction

1.1 Magnetic Reconnection

Magnetic reconnection converts magnetic energy into particle kinetic energy by magnetic field line contraction after a change of magnetic topology. It drives explosive energetic events in our solar system, including solar flares [8], Coronal Mass Ejections (CMEs) [9], and geomagnetic storms [10], which can have large impacts on the space weather environment and even power grids on Earth. It also drives the sawtooth crash in fusion device leading to disruption of confinement [11]. In addition, it has been proposed as a particle energization mechanism in other astrophysical contexts such as stellar flares [12], millisecond pulsars [13], the heliospheric current sheet [14, 15], pulsar wind nebulae [16, 17], black hole jets [18], etc. However, the conversion process from the magnetic field to high speed flows, heating and energetic particles remains only partially understood. In this dissertation, we emphasize the application to reconnection in the solar corona and inner heliosphere.

To introduce the basic concept of reconnection, we need to start from the frozen-in theorem. In ideal MHD theory, the electric field $\mathbf{E}$, the magnetic field $\mathbf{B}$, and the plasma fluid velocity $\mathbf{v}$ (approximately the ion fluid velocity) are related

through Ohm's law

$$\mathbf{E} + \frac{1}{c}\mathbf{v} \times \mathbf{B} = 0. \tag{1.1}$$

Plugging it into the Faraday's law, we get

$$\nabla \times (\mathbf{v} \times \mathbf{B}) = \frac{\partial \mathbf{B}}{\partial t}. \tag{1.2}$$

By integration, this implies that the magnetic flux through a closed contour moving together with the plasma will be conserved. This is equivalent to a intuitive statement that the plasma is frozen onto the field lines and moves together with the field lines. Any two fluid elements connected by a field line will always be connected by the same field line and, hence, a change in magnetic topology is forbidden in ideal MHD. For magnetic reconnection to happen, there needs to be some non-ideal effects.

From the basic electron equation of motion in two fluid MHD theory

$$m_e \frac{d\mathbf{v_e}}{dt} = -e\mathbf{E} - e\frac{1}{c}\mathbf{v_e} \times \mathbf{B} - \frac{1}{n}\nabla \cdot \mathbf{P_e} - m_e \nu_{ei}(\mathbf{v_e} - \mathbf{v}), \tag{1.3}$$

we can derive the generalized Ohm's law:

$$\mathbf{E} + \frac{1}{c}\mathbf{v} \times \mathbf{B} = \eta \mathbf{j} + \frac{\mathbf{j} \times \mathbf{B}}{nec} - \frac{1}{ne}\nabla \cdot \mathbf{P_e} + \frac{m_e}{e}\frac{d\mathbf{v_e}}{dt}. \tag{1.4}$$

Here m_e is the electron mass, $\mathbf{v_e}$ the electron fluid velocity, e the elementary charge, c the speed of light, n the density, $\mathbf{P_e}$ the electron pressure tensor, ν_{ei} the ion electron

collision frequency, η the resistivity, $\mathbf{j}$ the current density and $d/dt = \partial/\partial t + \mathbf{v_e} \cdot \nabla$. We see that there are several terms on the right hand side that do not appear in the ideal Ohm's law. Those are the terms potentially capable of breaking the frozen-in condition and allowing magnetic topology to change.

The first term of interest is the resistivity term $\eta\mathbf{j}$. Historically, the Sweet-Parker model was the first theory of resistive reconnection [19, 20]. In Figs. 1.1, magnetic fields pointing in opposite directions are separated by a thin current sheet with a length on the order of the system size. Plasma frozen onto the field flows from above and below into this current sheet. In this current sheet region, the resisitivity term takes effect and breaks the frozen-in condition. The field is then able to break and reconnect and the magnetic tension of the highly bent reconnected field line will drive plasma to flow out from the two sides with the Alfvén speed $c_A = B/\sqrt{4\pi n m_i}$. The expelled plasma will leave a lower pressure in the current sheet region and will draw in more plasma from upstream. So this is a self driven process. This region where the frozen-in condition is broken is called the diffusion region. The problem with this model is that the upstream plasma all has to go through this thin long nozzle of the diffusion region to go downstream, which makes the reconnection slow. With the low collisionality and thus low resistivity in space plasmas, it turns out that the reconnection in this model will take weeks to complete a solar flare, which usually only last for minutes or hours. So it is way too slow to explain the fast energy release observed in the solar flares.

To address this, Petschek proposed a model that now carries his name [21], which assumed that the diffusion region can be much shorter than the system size.

As shown in Figs. 1.2, most of the upstream plasma does not go through the small diffusion region in the center, but through a pair of standing slow shocks on each outflow which connect to the diffusion region and open up like a fan. Plasma from upstream goes through the shock and gets accelerated to flow out with the Alfvén speed (red arrows). With a opened up outflow, this configuration is capable of achieving a fast reconnection rate. However, this configuration can not be sustained in a MHD simulation with uniform resistivity and it will return to the elongated Sweet-Parker configuration [22]. The Petscheck configuration can only be realized if the resistivity is localized at the diffusion region [23]. Whether this can be achieved by anomalous resistivity due to current driven turbulence in the diffusion region is still under investigation [24–26].

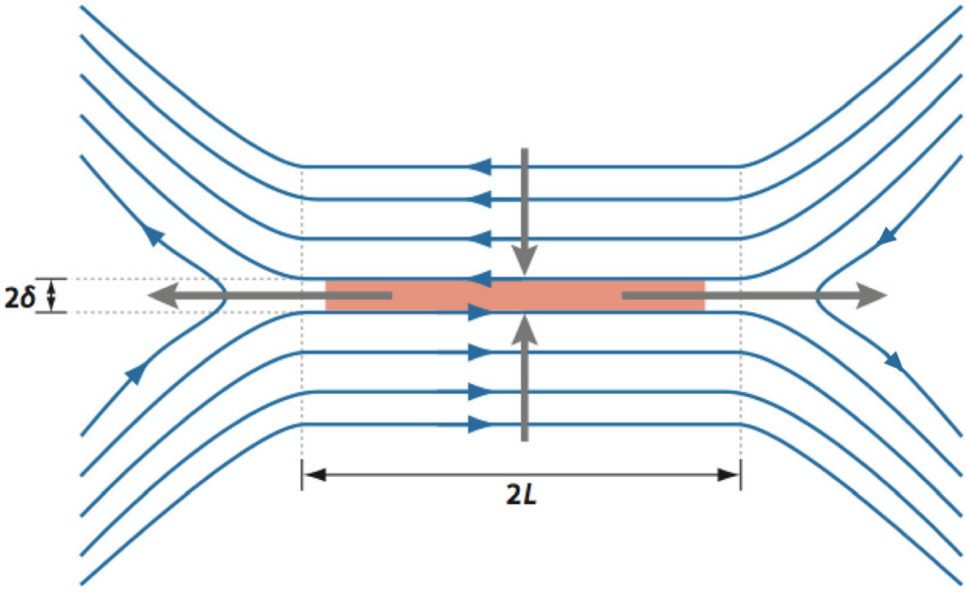

Figure 1.1: A schematic picture of the Sweet-Parker reconnection model. (Reprinted with permission from Ref. [Yamada, 2015] [1]. ©2015 AIP Publishing LLC.)

More recently, it has been found that the collisionless terms in the generalized Ohm's law can also lead to reconnection. If the diffusion region width get thinner

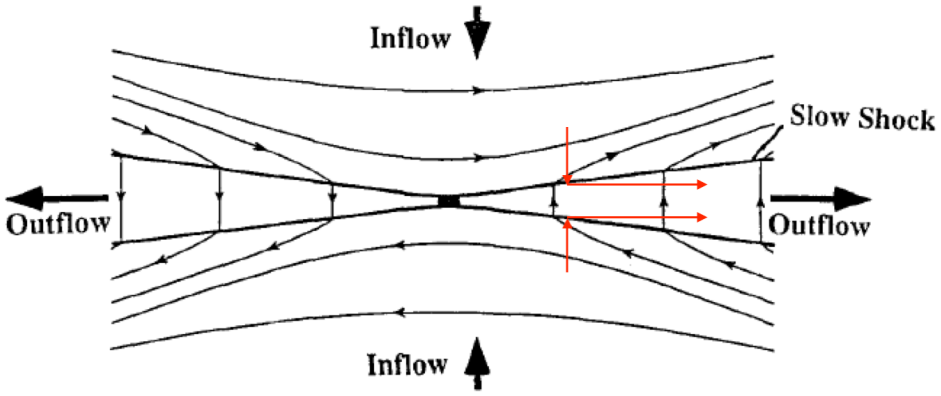

Figure 1.2: A schematic picture of the Petscheck reconnection model. (Reprinted with permission from Ref. [Lin et al., 1993] [2]. ©1994 Kluwer Academic Publishers.)

than the kinetic scale d_i (the ion inertial length), the Hall term $\mathbf{j} \times \mathbf{B}$ will become larger than the $\mathbf{v} \times \mathbf{B}$ term and ions decouple from the electrons and magnetic fields. This d_i scale can be seen by balancing these two terms:

$$\frac{1}{c}|\mathbf{v} \times \mathbf{B}| \sim \frac{c_A B}{c} < \frac{|\mathbf{j} \times \mathbf{B}|}{nec} \sim \frac{B^2}{4\pi ne\delta}, \tag{1.5}$$

where δ is the width of the current sheet. We then get $\delta < d_i$. This region where the ion frozen-in condition is broken is called the ion diffusion region. However, the Hall term itself does not break the electron frozen-in condition since the original Ohm's law plus the Hall term is just equivalent to the electron frozen-in condition

$$\mathbf{E} + \frac{1}{c}\mathbf{v_e} \times \mathbf{B} = 0. \tag{1.6}$$

So the electron diffusion region is at an even smaller electron scale d_e (the electron inertial length), where other collisionless terms in the generalized Ohm's law break

the electron frozen-in condition. In collisionless reconnection, the ion diffusion region has a length of about only 10 d_i, which is usually much smaller than the system size. Such a small diffusion region can realize the configuration of the Petscheck model and thus explain the fast reconnection in solar flares. In this configuration, since the diffusion region is small, most of the magnetic energy is released downstream of the diffusion region when the field lines contract and shoot like a slingshot.

Though the reconnection configuration discussed in this section has only in-plane magnetic fields (antiparallel reconnection), in general there can be an additional out-of-plane field which is called the guide field.

1.2 Reconnection in the Corona and Inner Heliosphere

One of the long lasting puzzles in astrophysics is how the corona gets heated to a few million degrees Kelvin, so much hotter than the photosphere (∼6000K). The corona is magnetically dominated and the β is low (β is the ratio of plasma thermal pressure to magnetic pressure). The energy of particle heating comes from the magnetic field energy. Magnetic reconnection is one of the most promising mechanisms for such energy conversion. In fact, reconnection is ubiquitous in the corona and the inner heliosphere. It can happen in solar flares, in helmet streamers higher in the corona [27], and at current sheets in the inner heliosphere. For example, Fig. 1.3 shows the magnetic field squashing factor Q at 10 solar radii based on a corona magnetic field model [3]. Q is a measure of the distortion of magnetic flux tubes in the magnetic field mapping from photosphere to a certain radius and is directly

related to the gradients in the magnetic field connectivity [3, 28, 29]. Therefore, it is large at magnetic separatrices, where current sheets form and reconnection can happen. Thus the high Q filament regions in the figure indicate the formation of many current sheets and suggest that reconnection is common there. Also, it was suggested by Parker [30] that a large number of nanoflares, which are very small reconnection events, are adequate to power the corona heating.

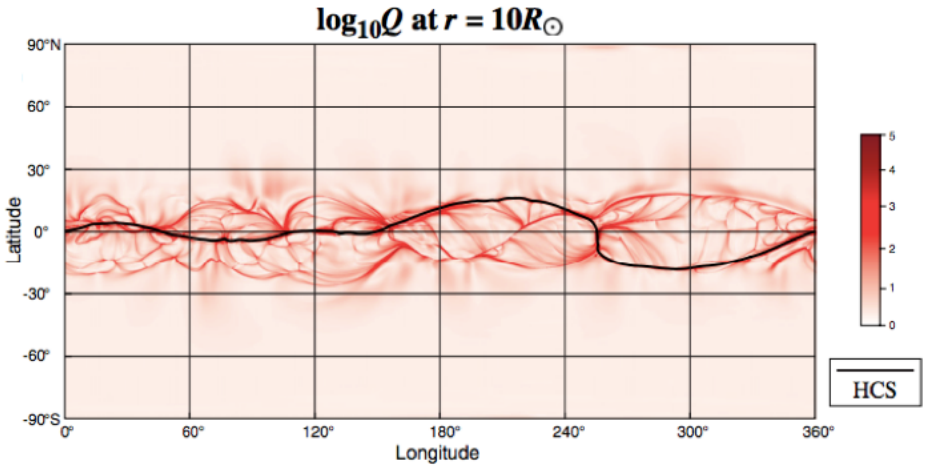

Figure 1.3: The squashing factor Q on a logarithmic scale at ten solar radii over longitude and latitude. (Reprinted with permission from Ref. [Antiochos et al., 2011] [3]. ©2011 American Astronomical Society.)

Here we introduce the canonical picture of a solar flare inferred from observations by Tsuneta [4] (Fig. 1.4). This picture is based on the Petscheck reconnection model. After the reconnection occurs at the x-line, according to the Petscheck model, plasma will be heated between two slow shocks and flow out with the Alfvén speed both upwards to the space and downwards to the photosphere. The upward flowing plasma sometimes launches as a CME, although here we focus on the downward flow region. In this region, Tsuneta suggests that due to heat conduction along field lines, the two hot ridges in the figure connected to the slow shocks also get heated

and the downwards fast flows cool down. The flows frozen in the field lines eventually stop at the bottom and become a loop filled with evaporated plasma from the photosphere, emitting soft x-rays. As an example, an x-ray image of loops from a typical solar flare from the TRACE satellite is shown in Fig. 1.5. In addition, recent high resolution hard x-ray observations by Reuven Ramaty High Energy Solar Spectroscopic Imager (RHESSI) show that in some large flares, a super hot hard x-ray source can be found above the loop top. It can have an electron temperature an order of magnitude higher than the corona temperature and have energetic electron power law tail up to the order of MeV energy [31–33]. Examining whether a single x-line solar flare picture can explain such strong electron energization is one of the goals of this dissertation.

1.3 Particle Heating Studies in Reconnection

How plasma gains energy during reconnection has previously been analyzed numerically with both fluid and kinetic descriptions. Sophisticated MHD simulations can employ computational domains of coronal scales and provide direct comparisons to observations [34,35], but do not distinguish between the heating of electrons and ions and require assumptions on particle velocity distributions, isotropy, viscosity and heat flux without capturing many potentially important kinetic effects. Capturing such effects from first principles requires full particle kinetic descriptions. Previous studies with full particle models are typically localized near the reconnection diffusion regions [36,37] or explore outflows from single [38–43] or multiple

reconnection sites [6, 44, 45]. This dissertation mostly focuses on the outflow from a single reconnection site, which is the case in the canonical flare picture, although we will briefly introduce the multiple reconnection sites scenario in Section 1.6. Observations of reconnection exhausts in the magnetosphere [46, 47] find an empirical linear scaling for ion and electron heating as a function of the available magnetic energy per particle, which is consistent with that found in kinetic simulations [39]. However, these studies only explored the β of order unity regime. The mechanism of electron heating is under investigation and debate [40, 41].

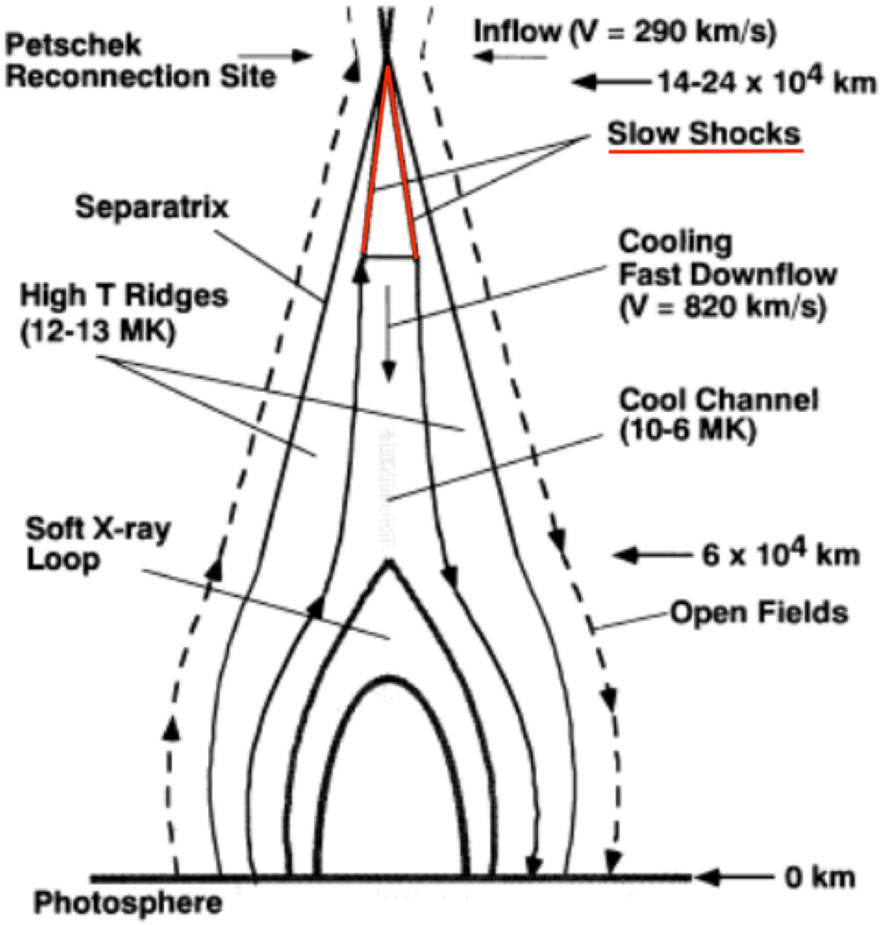

Figure 1.4: The canonical picture of solar flares inferred from observations. (Adapted with permission from Ref. [Tsuneta, 1996] [4]. ©1996 American Astronomical Society.)

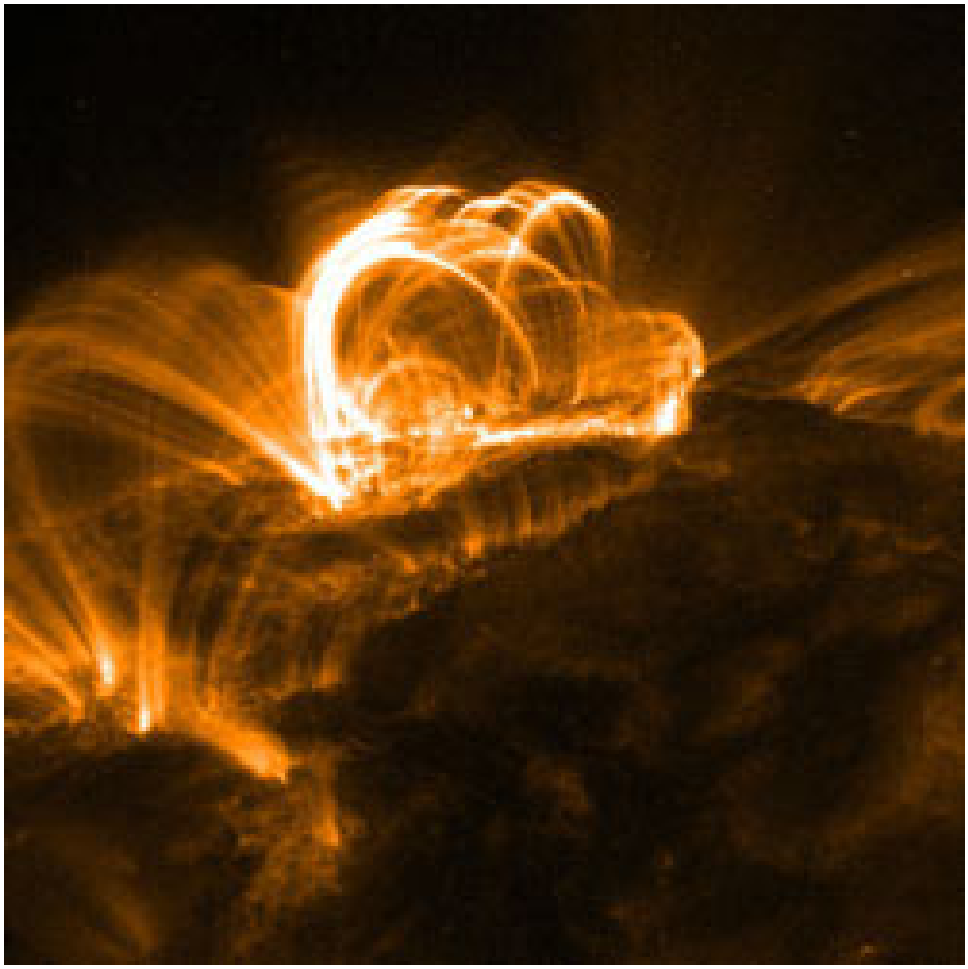

Figure 1.5: Image of soft X-ray loops created by a typical solar flare, which was captured by NASA's TRACE satellite in September 2005. Credits: NASA/LMSAL.

An important step in understanding the heating mechanism in reconnection exhausts is the discovery of a parallel electric potential that exists even far downstream of the diffusion region. As seen in Fig. 1.6 from Egedal et al. [5], the middle of the exhaust contains a parallel electric potential whose magnitude can be found by integrating the parallel electric field along field lines beginning from the ambient plasma. This potential confines electrons in the exhaust and energizes electrons that come into the exhaust. For the ions, if we jump to the frame of the Alfvénic

outflow, the ambient ions will have a Alfvén velocity in the opposite direction. With the component of this velocity parallel to the field, they flow into the exhaust from both sides along the field line and form counterstreaming beams in the exhaust to produce ion heating [43]. Haggerty et al. found that the parallel potential will slow down the incoming ions and reduce the ion heating [40]. Such a potential governs the heating partition between ions and electrons but the mechanism that determines the magnitude of this potential is only partially understood. Since reconnection in the corona typically has a guide field, in this dissertation we will look at particle heating in guide field reconnection exhausts and explore the structure and magnitude of the potential.

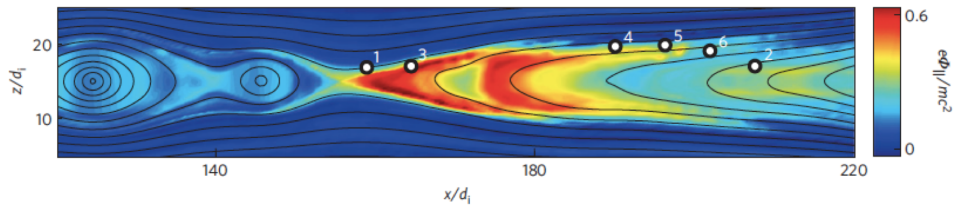

Figure 1.6: Positive parallel electric potential in the exhaust that exists even far downstream of the x-line. (Reprinted with permission from Ref. [Egedal et al., 2012] [5]. ©2012 Macmillan Publishers Limited.)

1.4 Particle-in-Cell Simulation

The numerical code we use in this dissertation is the particle-in-cell (PIC) code `p3d` [48]. A PIC code tracks the evolution of the position and velocity of particles evolving in electromagnetic fields via the Newton-Lorentz equations of motion. The fields are advanced via Maxwell's equations. In practice, the fields are known on a lattice in which each grid cell contains many particles. During each time step,

the values of the electromagnetic fields are stored on the gridpoints, which, after appropriate interpolation, controls the particle motion in the grid cells through the Newton-Lorentz equations. Then the moving particles can distribute their mass and current onto the grids as density and current density to help evolve the field through Maxwell's equations. The updated field can then control the particle motion again in the next time step. This repeated process models the evolution of a kinetic physical system. However, the number of particles per grid cell in the simulation is usually orders of magnitude smaller than in nature, while each particle would carry proportionally more mass and charge as a macroparticle. The typical number of particles per grid cell we use is 100. While the macroparticles can still describe the physical evolution, they make the phase space less smooth and create more numerical noise in the system. The noise sometimes makes the information less clean and can even create unphysical particle scattering. These negative effects can only be reduced by increased resolution or increased number of particles per cell.

An explicit PIC code like `p3d` needs to resolve certain kinetic space and time scales to maintain numerical stability. These scales include the Debye length, the electron inertial length, the Langmuir frequency, the electron cyclotron frequency, etc. In addition, it needs to satisfy the Courant-Friedrichs-Lewy (CFL) condition, which means that any signal propagating through the simulation must pass through less than one grid cell during a timestep. The typical speeds of a signal in plasma include the speed of light, the Alfvén speed, the electron thermal speed, etc. Such high speeds will further limit the timestep that can be used. A high spatial and temperal resolution is required to satisfy all these criteria while the interesting phys-

ical phenomena occur on much larger scales. This makes such PIC simulations very expensive. To reduce the separation of scales, several tricks are usually employed. The ion-to-electron mass ratio used in simulations, though much larger than one, is often much smaller than the real value, 1836. The ratio of the speed of light to other speeds is also often artificially reduced, though it is still large enough so the particles remain nonrelativistic. These tricks make the simulations affordable, but one needs to be very careful that these tricks are not over applied to alter the real physics being investigated in nature.

1.5 Riemann Simulation

As discussed in the previous section, conventional kinetic reconnection simulations usually have high computational cost compared to fluid simulations. Due to such constraints, the kinetic simulation results are often limited to low artificial ion-to-electron mass ratios with computational domains that are at most several hundred d_i in size. High mass-ratio and low β simulations typically have smaller computational domains because of the requirement in particle-in-cell (PIC) models that the Debye length be resolved. Some of such drawbacks can be addressed, in part, by employing quasi-1D particle-in-cell Riemann simulations so that the spatial scale along the inflow direction can be dramatically increased, the upstream plasma β can be reduced and the mass ratio can be increased. This is particularly useful in low β systems like the corona since a near-realistic ion-to-electron mass ratio is necessary to keep the electron thermal speed much greater than the Alfvén speed

(as it is in the corona). Riemann simulations model reconnection outflows in order to study the physics of particle heating downstream of the ion diffusion region. The magnetic geometry of a Riemann simulation resembles a single reconnection outflow from the x-line. It reduces the dimension of a 2D outflow by neglecting the weak dependence on the outflow direction, thus transforming it into a 1D problem. The time development of the 1D Riemann simulation is a proxy for the time development of the reconnection exhaust in the frame of the outflow. Since, in the frame of the outflow, the exhaust expands in width, the results of a Riemann simulation expand over time as well. As illustrated in Fig. 1.7, different times in the Riemann simulation correspond to different distances from the x-line. During reconnection, the magnetic energy is mostly dissipated downstream of the reconnection site, where the field lines contract, so it is not necessary to simulate the reconnection diffusion region in order to capture the physics of particle heating in a large-scale system. Instead, the contracting field lines in a Riemann simulation will uncover the physical processes of particle heating in a single reconnection outflow.

Riemann simulations have been used to explore the structure of the exhaust but were not used to investigate particle heating and in particular the relative heating of electrons and ions. They were based on MHD models [2], hybrid simulations [49–52] as well as PIC simulations [53, 54] without a guide field. The MHD models have explored both antiparallel and guide field exhausts [2]. In the case of antiparallel reconnection, the expanding exhaust consists of two back to back slow shocks moving outwards from the center over time (see Fig. 1.8). The profiles in the figure show the increase of temperature and velocity between the two slow shocks,

which is consistent with the Petscheck model. In the guide field case, the exhaust has a pair of rotational discontinuities (RD) and a pair of slow shocks (SS) moving from the center with their own constant speeds (see Fig. 1.9). Plasma gains velocities between the RD and SS while the heating occurs only between the two SSs. In MHD theory, an RD is a discontinuity across which the magnetic field changes direction while the field strength, plasma density and pressure is unchanged. A SS is a shock across which the plasma flow drops from above the slow magnetosonic speed to below the slow magnetosonic speed, accompanied by a simultaneous decrease in magnetic field strength and increase in the plasma density and pressure. What will be different about the structures in a kinetic description is to be answered in this dissertation. On the other hand, Riemann simulations do not address the physics of multi x-line reconnection since they only model one reconnection outflow. We will briefly introduce the multi x-line reconnection scenario in the next section.

1.6 Multi X-line Reconnection

In the previous sections, we mostly focused on heating in a single reconnection exhaust, which is the scenario in the canonical solar flare picture. However, since the diffusion region is small, if the reconnection current sheet is long enough, there can be multiple x-lines reconnecting on a current sheet at the same time. This is the multi x-line reconnection scenario. In a 2D case, each two adjacent x-lines produce outflows towards each other, forming a magnetic island in between. So the multiple x-line will break the current sheet into multiple islands. For example, Dahlin et al. [6]

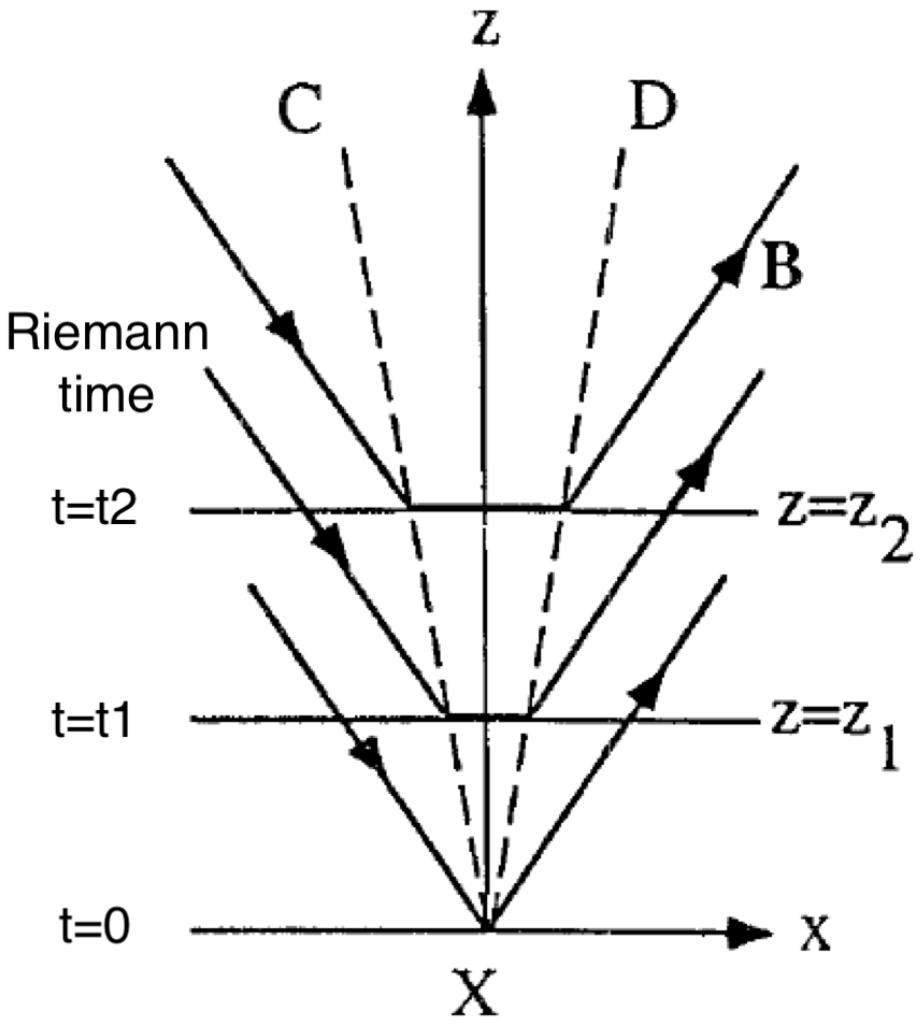

Figure 1.7: Illustration of different Riemann simulation time corresponding to different distance from the x-line. (Adapted with permission from Ref. [Lin et al., 1993] [2]. ©1994 Kluwer Academic Publishers.)

performed a 2D particle-in-cell simulation as seen in Fig. 1.10. There are two current sheets in the domain and each one breaks into multiple islands. After the formation of these islands, the adjacent islands can further reconnect with each other and merge into bigger and bigger islands. Each merger of islands is accompanied by contraction of field lines and release of magnetic energy. During this process, particles are bounced between the two ends of the contracting island and are accelerated by the

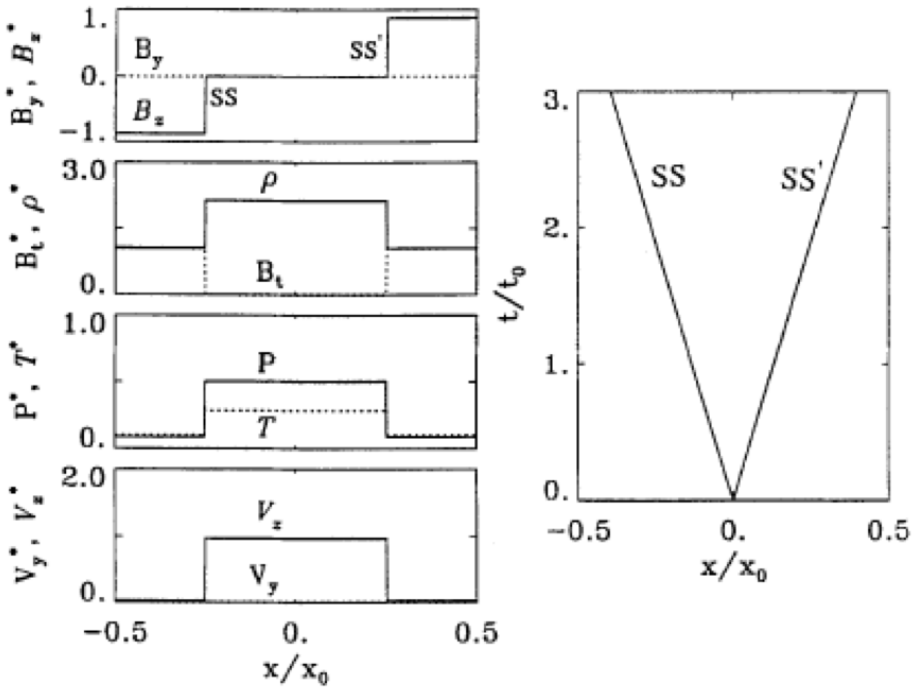

Figure 1.8: Profiles of MHD antiparallel Riemann problem results and space time diagram of SSs. (Reprinted with permission from Ref. [Lin et al., 1993] [2]. ©1994 Kluwer Academic Publishers.)

first order Fermi acceleration. Therefore the continuous mergers of islands could accelerate particles to higher and higher energy. In three dimensions, the field lines become more chaotic and transport the electrons more efficiently. As a result, the energetic electrons get even more chances to be accelerated [45]. Although we do not focus on the multiple x-line reconnection in this dissertation, it is an important alternative mechanism to compare with.

1.7 Summary of Results

Here and below, the coordinate system is defined to be: x the outflow direction; y the inflow direction; z the guide field direction.

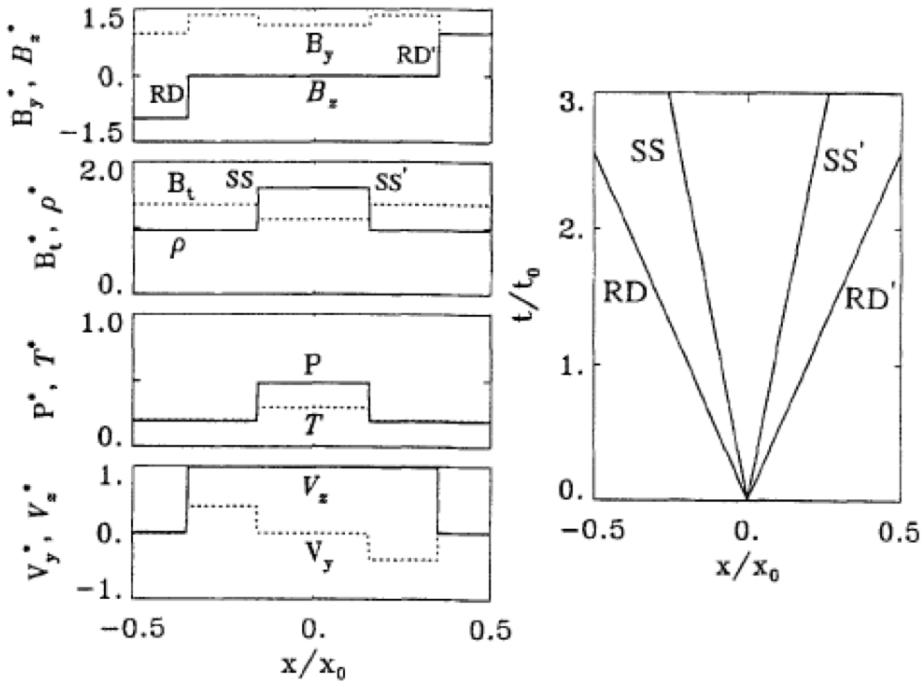

Figure 1.9: Profiles of MHD guide field Riemann problem results and space time diagram of RDs and SSs. (Reprinted with permission from Ref. [Lin et al., 1993] [2]. ©1994 Kluwer Academic Publishers.)

This dissertation first explores the heating mechanism for ions and electrons as well as partition of the energy released in large scale low β reconnection exhausts with a guide field. The heating mechanism is mostly controlled by laminar physics, although the simulations are restricted to 2D (y-z) and the full development of turbulence in 3D is not captured. In order to understand more fully the role of turbulence in this process, we then explore in greater depth the dynamics of instabilities and turbulence in 2D (x-y) and 3D exhausts.

In chapter 2, we present investigations of particle heating in low β reconnection outflows downstream from a single x-line through PIC Riemann simulations. In these simulations the ratio of the guide field to the reconnecting component of the

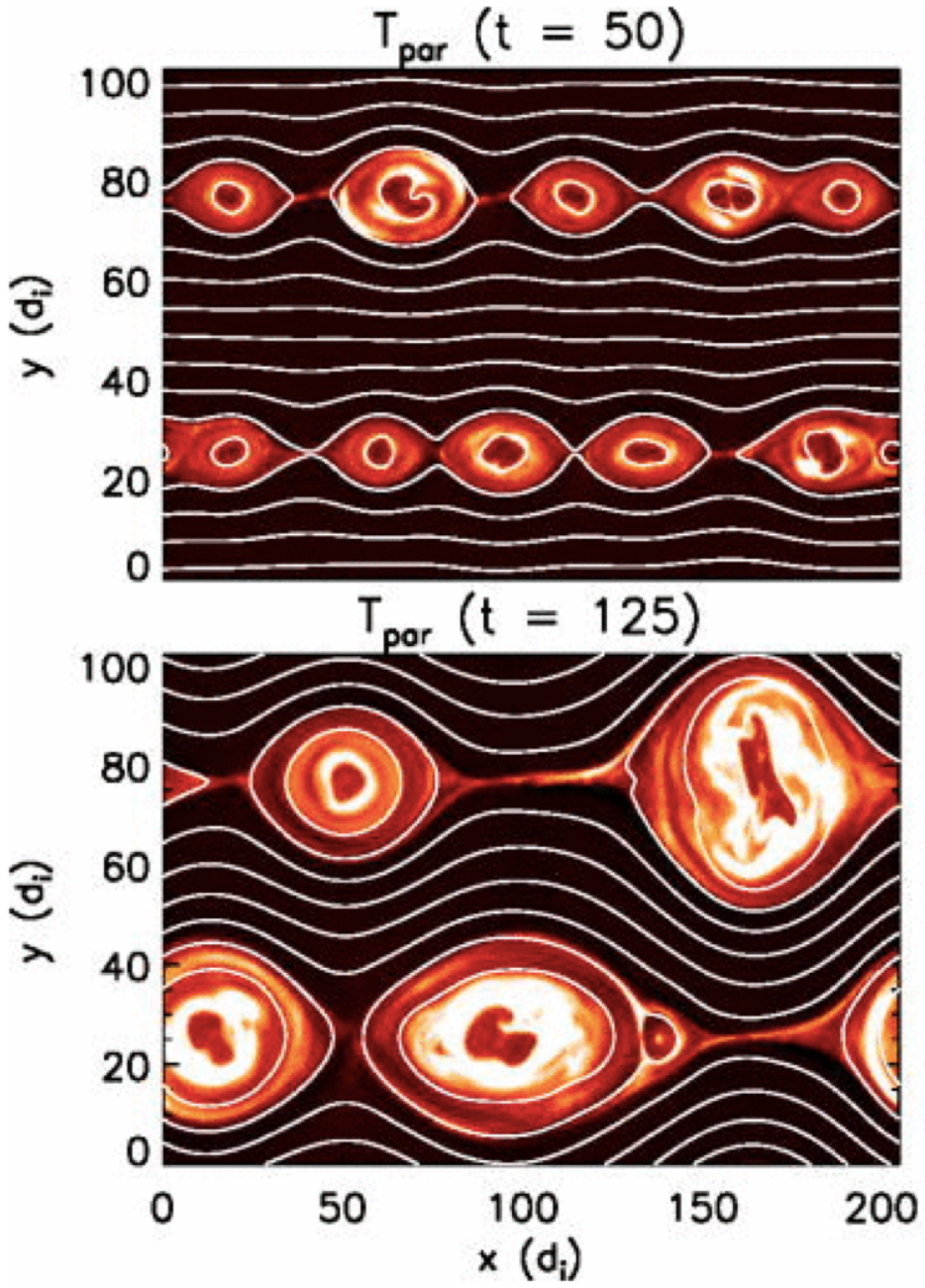

Figure 1.10: Parallel electron temperature results of a multiple x-line reconnection simulation at two different times. Electrons are being energized in merging magnetic islands. (Reprinted with permission from Ref. [Dahlin et al., 2014] [6]. ©2014 AIP Publishing LLC.)

field is taken to be of the order of or greater than unity. As in the MHD model we find that there are two rotational discontinuities (RD) that bound the exhaust and

two slow shocks (SS) that develop within the exhaust. The ions are accelerated at the RDs and form counterstreaming beams downstream of the SSs. However, these counterstreaming beams are stable so that turbulence within the entire exhaust remains weak and as a result SSs produce little dissipation, an important difference from the MHD description. Downstream of the SSs the counterstreaming ion beams produce an increase in their density (by about a factor of two). A positive potential in the region downstream of the SSs develops to confine the downstream electrons in this high density region. The electrons are accelerated by the potential from upstream of the SS to downstream of the SS and are partly trapped by the potential in the region between the two SSs. Electron trapping by this potential modestly increases the downstream electron temperature.

In a series of simulations carried out with increasing upstream magnetic energy per particle (at fixed upstream temperature) the ion downstream temperature increases in a linear manner, proportional to the available magnetic energy, while the electron temperature plateaus, increasing only modestly from the upstream value. This is because the electron heating is limited by the amplitude of the potential across the SSs. A very large potential does not develop because it would trap too many electrons compared with the modest increase in ion density and so charge neutrality would be violated. The SSs in the simulations remained laminar and neither species undergoes the canonical diffusive shock acceleration at the SSs since no turbulence scatters particles back and forth across the shocks. Most of the released magnetic energy goes into ions driven at the RDs as the bulk reconnection outflow or as the counterstreaming ion beams in the midplane of the exhuast, which are not

thermalized by the SSs.

In Chapter 3, we explore in much greater depth the instabilities and turbulence in low-β guide field reconnection exhausts to firmly establish the laminar nature of reconnection exhausts in this regime. We carry out a 2D (x-y) reconnection simulation and 2D (x-y) and 3D Riemann simulations with various mass-ratios. The guide field breaks the system's symmetry and leads to a density cavity at the RD on one side of the exhaust (the side where the electron velocity supporting the current across the RD points toward the midplane of the exhaust) and a density bump at the other RD. In 2D simulations the streaming electrons in the cavity of the RD drive the Buneman instability at early time but later in time the dominant instability movies to the core of the exhaust and leads to large amplitude striations in the electron parallel current with characteristic scales of order of the ion Larmor radius ρ_i. The instability is an ion cyclotron wave driven by the strong electron beam injected into the exhaust by the low density RD [55]. However, in 3D simulations the Buneman instability at the low density RD becomes much stronger (due to a non-zero k_z) so that the electron beam injected into the exhaust becomes much weaker and the development of the striations is suppressed. The result points to the importance of full 3D simulations of reconnection to understand the mechanisms for energy conversion. The 3D simulations also reveal the development of a weak ion-ion streaming instability within the exhaust which did not appear in the 2D model. All of these instabilities, Buneman, ion cyclotron and ion-ion streaming, become weaker with higher ion-to-electron mass ratio as the electron thermal speed becomes much greater than the Alfvén speed. The conclusion, therefore, is that

the instabilities and turbulence that develop are expected to be weak in a realistic low-β, guide-field reconnection exhaust. The dynamics of a single x-line exhaust is dominated by laminar processes described in Chapter 2.

Chapter 2: Particle Heating and Energy Partition

2.1 Overview

In this capter we present investigations of particle heating in low β reconnection outflows downstream from a single x-line through PIC Riemann simulations.

The organization of this chapter is the following: in Sec. 2.2, by comparing to the conventional reconnection simulations, we show that Riemann simulations are good proxies to model the heating in reconnection exhausts; in Sec. 2.3, we analyze the results of Riemann simulations and discuss the heating mechanisms for ions and electrons; in Sec. 2.4, we present a set of simulations to discuss the scaling of electron and ion heating and energy partition with increasing available magnetic energy; we finally present the conclusions and implications in Sec. 2.5.

2.2 Riemann simulations as proxies for reconnection outflows

2.2.1 Riemann simulations

The concept of Riemann simulations was introduced in Chapter 1.5. In practice, the computational domain of a Riemann simulation consists of a thin, long, quasi-1D box extended along the reconnection inflow direction, y, with the out-

flow direction, x, and guide field direction, z, short. We take all boundaries to be periodic. Although our domain contains two current sheets to achieve periodic boundaries in y, we only focus on one current sheet, as will be described later. The lengths of the two short dimensions (x and z) can be adjusted to include the wavelengths of the dominant instabilities if they are important. In this way, with the same computational cost, we can explore the physics of magnetic energy conversion and particle heating in a large spatial domain with low-β and and relatively high mass ratio. In contrast, with a conventional reconnection simulation, because the width to length ratio of the exhaust is around 0.1, it is a challenge to model a system that is large enough to separate the reconnection exhaust structures transverse to the outflow direction.

Because the coronal environment typically has low β, we use a force free configuration with a guide field where the initial magnetic field strength and density are constant but there is magnetic shear at the current sheet. The equilibrium is assumed to be symmetric across each current layer. We also use a small constant initial B_y (the reconnected component of the magnetic field) to provide the magnetic tension to drive the outflow. The equilibrium is defined as follows:

$$B_x = B_{\mathrm{x,a}}\ \tanh(y/w_0), \tag{2.1a}$$

$$B_z = \sqrt{(B_{\mathrm{x,a}}^2 + B_{\mathrm{z,a}}^2 - B_x^2)}, \tag{2.1b}$$

$$B_y = 0.1 B_{\mathrm{x,a}}, \tag{2.1c}$$

$$n = n_0, \tag{2.1d}$$

where the "a" subscript represents asymptotic upstream values.

We use the particle-in-cell code `p3d` in which the particle positions and velocities evolve via the Newton-Lorentz equations of motion [48]. The electromagnetic fields are advanced in time by Maxwell's equations. Magnetic field strengths are normalized to $B_{\mathrm{x,a}}$, densities to the initial density n_0, lengths to the ion inertial length $d_i = c/\omega_{pi}$ (based on n_0), times to the inverse ion cyclotron frequency Ω_{ci}^{-1}, velocities to the Alfvén speed C_{Ax} based on $B_{\mathrm{x,a}}$ and n_0, and temperatures to $m_i C_{Ax}^2$. The initial conditions used for all the simulations are shown in Table 2.1. After a Riemann simulation starts, the exhaust begins to form and expand in width, heating ions and electrons within it.

Run	m_i/m_e	$B_{x,a}$	$B_{z,a}$	$T_i = T_e$	dims	$L_y \times L_x \times L_z$	c^2	dx	dt
1	25	1	1	0.05	2	102.4×409.6 × 0	45	0.0125	5.9e-3
2	25	1	1	0.05	1	102.4×0.2×0	45	0.0125	5.9e-3
3	400	1	2	0.02	2	22.9×0×0.54	720	0.0007	2e-4
4	100	1	2	0.02	2	22.9×0×1.08	180	0.0014	6e-4
5	400	1	2	0.02	1	22.9×0×0.011	720	0.0007	2e-4
6	400	$1/\sqrt{20}$	$1/\sqrt{20}$	0.005	1	45.8×0×0.0022	720	0.00056	1.56e-4
7	400	$\sqrt{0.125}$	$\sqrt{0.125}$	0.005	1	45.8×0×0.0022	720	0.00056	1.56e-4
8	400	$\sqrt{0.25}$	$\sqrt{0.25}$	0.005	1	45.8×0×0.0022	720	0.00056	1.56e-4
9	400	$\sqrt{0.5}$	$\sqrt{0.5}$	0.005	1	45.8×0×0.0022	720	0.00056	1.66e-4
10	400	$\sqrt{0.75}$	$\sqrt{0.75}$	0.005	1	45.8×0×0.0022	720	0.00056	1.56e-4
11	400	1	1	0.005	1	45.8×0×0.00186	720	0.000466	1.3e-4
12	800	$\sqrt{2}$	$\sqrt{2}$	0.005	1	45.8×0×0.0011	1440	0.00028	5.5e-5
13	1600	1	2	0.02	1	22.9×0×0.00447	2880	0.00028	4e-5
14	400	1	2	0.02	1	45.8×0×0.011	720	0.0007	2e-4

Table 2.1: Simulation parameters

2.2.2 Comparison with a reconnection simulation

Here we show that with the same parameters, Riemann simulations produce comparable results to conventional reconnection simulations. Some results of a conventional 2D reconnection simulation (Run 1) with a guide field the same as the reconnecting field are shown in Fig. 2.1. All data from Run 1 have been smoothed to reduce the noise. In Fig. 2.1(a), the in-plane magnetic field lines are overplotted on J_z. Well downstream of the x-line, the field lines turn sharply from the x to the y direction, indicating that the reconnecting field B_x sharply drops to nearly zero. Note, however, that there is a strong guide field B_z so that within the exhaust the magnetic field points dominantly in the z direction. This feature is characteristic for guide field reconnection but is absent in antiparallel reconnection where Petschek's switch-off shocks are suppressed because of pressure anisotropy [38]. J_z peaks at the exhaust boundaries to support this field change. Between regions of high current is the exhaust where plasma reaches the Alfvén speed C_{AX}, as shown in Fig. 2.1(b). Ions in the exhaust are heated as shown by the ion parallel temperature increase shown in Fig. 2.1(c). In Fig. 2.2, we compare this 2D reconnection simulation (Run 1) to a 1D Riemann simulation (Run 2) with otherwise the same parameters. The second short dimension x in Run 2 is a dummy dimension that is included in the simulations but can be averaged to reduce noise. Fig. 2.2(a) shows $T_{e\|}$ of the outflow from the reconnection simulation. The green cut shows the location of the profiles of parallel electron and ion temperatures shown in Fig. 2.2(b). Fig. 2.2(c) shows the corresponding profiles from the Riemann simulation at the time when the exhaust

width is close to that in Fig. 2.2(b). In this chapter profiles along y from Riemann simulations with a short dimension in x have all been averaged over x to reduce noise. Similarly, we compare velocity, magnetic field and density profiles in Fig. 2.3 and Fig. 2.4. The comparable results from both types of simulations suggest that Riemann simulations are good proxies for the structure of outflows from conventional reconnection simulations. In the next section the structure of reconnection outflows will be discussed in more detail using Riemann simulations.

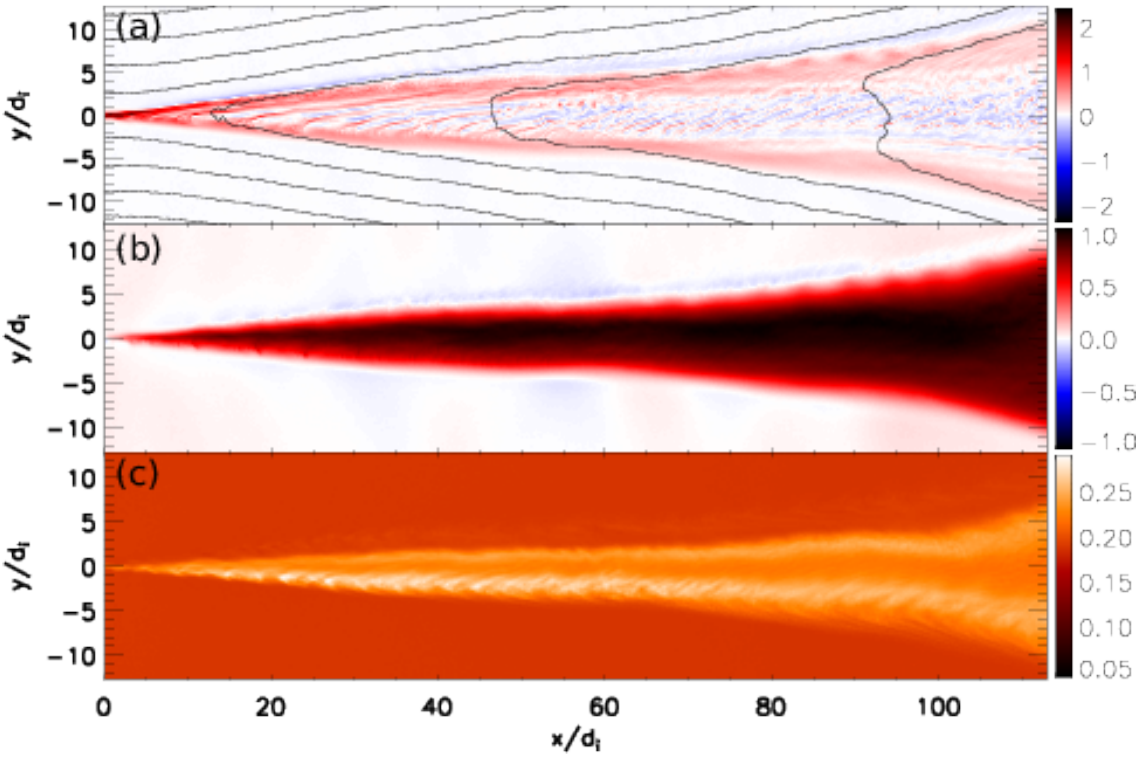

Figure 2.1: The exhaust of a 2D reconnection simulation (Run 1). (a) J_z with in-plane magnetic field lines overploted, (b) V_{ix}, (c) $T_{i\|}$.

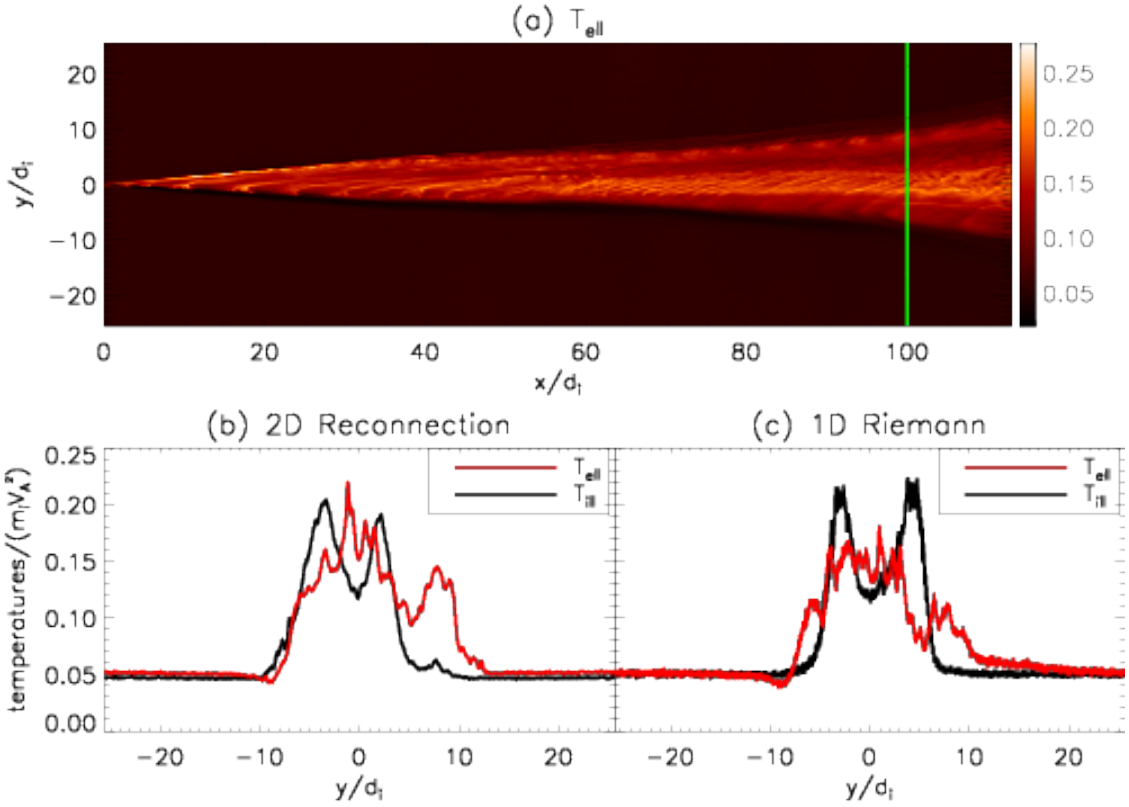

Figure 2.2: Comparing a 2D reconnection simulation and a 1D Riemann simulation. (a) $T_{e\|}$ of the 2D reconnection simulation (Run 1) exhaust, (b) profiles of $T_{e\|}$ and $T_{i\|}$ taken at the green line of (a), (c) the same profiles from the corresponding 1D Riemann simulation (Run 2).

2.3 Results and discussion

2.3.1 Overview

In this section, we analyze a 2D Riemann simulation (Run 3), which has a guide field twice the reconnecting field, in detail to show an example of typical results. This simulation has a second dimension along z, the dominant magnetic field direction within the exhaust, that is long enough to capture field-aligned streaming instabilities, which will be discussed in greater detail later. After the simulation begins, the ion and electron temperatures in the exhaust increase quickly and reach

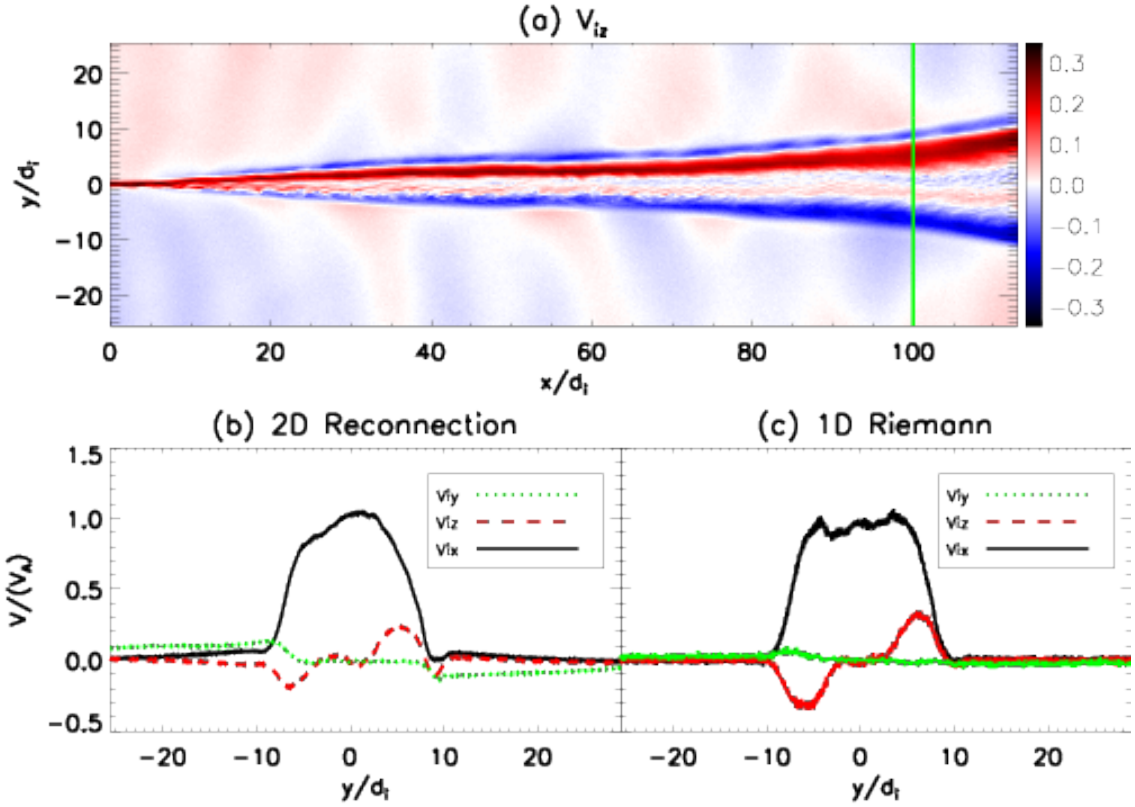

Figure 2.3: Similar to Fig.2, (a) V_{iz} of the 2D reconnection simulation (Run 1) exhaust, (b) profiles of V_{ix}, V_{iy} and V_{iz} taken at the green line of (a), (c) the same profiles from the corresponding 1D Riemann simulation (Run 2).

nearly constant values. Then as the exhaust expands over time, the profiles of temperature and other quantities expand steadily with their shape and magnitude nearly unchanged, resulting in more and more heated particles. Snapshots of the profiles of the magnetic field, the parallel electron and ion temperatures, the bulk flows and electron and ion densities are shown in Figs. 2.5 and 2.6.

The expanding exhaust consists of nonlinear structures propagating at constant speeds away from the initial central current sheet. They are two rotational discontinuities (RDs), where magnetic fields rotate, and two slow shocks (SSs), where the fluid velocity decelerates from above to beneath the slow sonic speed (~ 0.2 upstream of the shock). The structures are moving away from the midplane at nearly

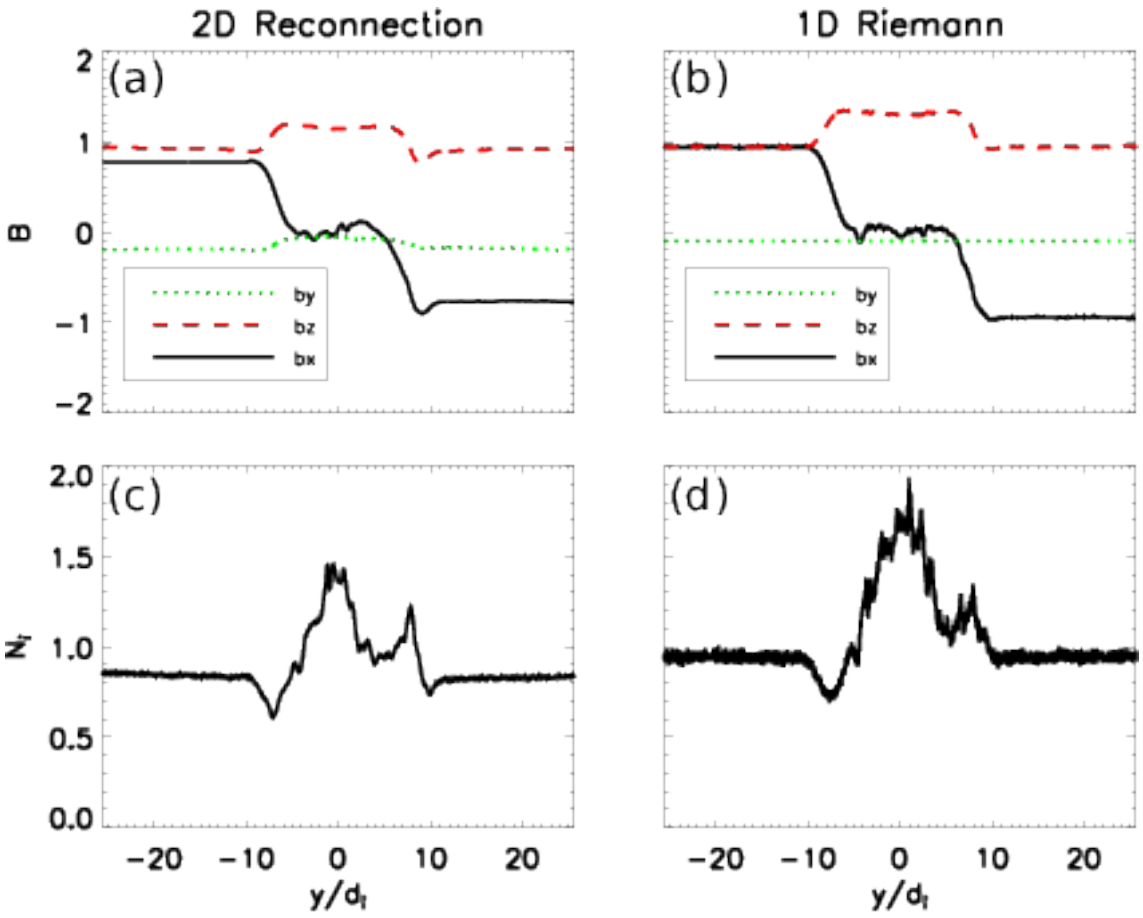

Figure 2.4: On the left, the profiles of B_x, B_y, B_z (a) and N_i (c) from the 2D reconnection simulation (Run 1). On the right, the profiles of B_x, B_y, B_z (b) and N_i (d) from the 1D Riemann simulation (Run 2).

constant speeds. With a sufficiently large guide field and sufficiently low β (in the case of the guide field equal to the reconnecting field, for example, $\beta \sim 0.01$), the RDs and SSs are clearly separated. An ideal MHD Riemann simulation also develops these structures [2], but the detailed properties will differ from those seen here because of the assumptions in MHD as discussed previously.

In Figs. 2.5 and 2.6 we present profiles of various quantities during the exhaust expansion. In Fig. 2.5(a) there is magnetic rotation at each RD (with magnetic field strength nearly unchanged) with the magnetic fields being nearly uniform through-

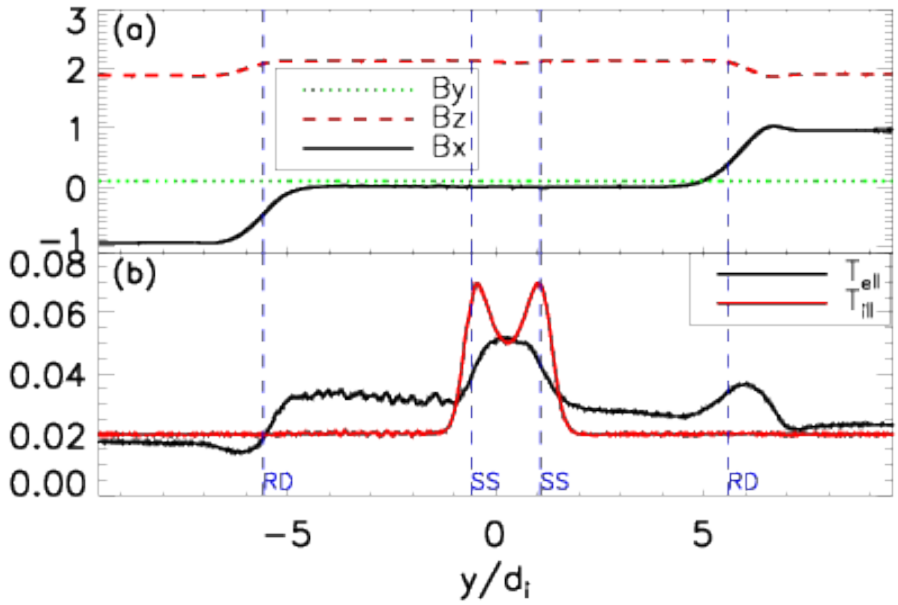

Figure 2.5: Profiles of B_x, B_y, B_z (a) and $T_{e\|}$ and $T_{i\|}$ (b) from the 2D Riemann simulation (Run 3).

out the region between the RDs. In Fig. 2.5(b), the strongest ion and electron parallel temperature increase is between the two SSs but there is also electron parallel heating between the RD and the SS, forming two shoulders in the electron parallel temperature profile. The perpendicular temperature change is negligible due to magnetic moment conservation and is therefore not shown. In Fig. 2.6(a) V_{ix} increases across the RDs and remains nearly constant across the entire exhaust, consistent with the MHD model. V_{iz} increases across each RD with opposite signs on either side of the exhaust. The resulting counterstreaming flows decreases to nearly zero across the SSs, again consistent with the MHD model. In Fig. 2.6(b), quasi-neutrality is well satisfied. The density has a cavity on one RD and a bump

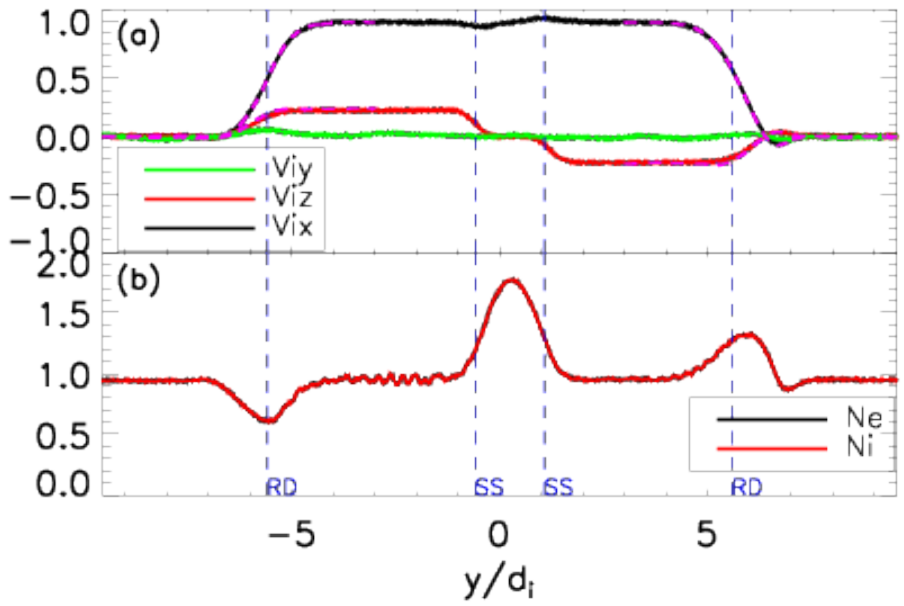

Figure 2.6: Profiles of V_{ix}, V_{iy} and V_{iz} (a) and N_e, N_i (b) from the 2D Riemann simulation (Run 3). The vertical dashed lines indicate the locations of the RDs and SSs. The purple dashed lines in (a) is the MHD model predictions in Equation (2.1) of V_{ix} and V_{iz} for comparison.

on the other one. The density does not change much across the RDs, while there is a peak between two SSs.

We integrate the parallel electric field (smoothed over one plasma period to reduce fluctuations) to obtain the parallel electric potential as shown in Fig. 2.7(a) and a zoom-in of the region between the SSs in (b). Note the separate localized variations of the potential at each RD and SS. The potential gradient drives the parallel current that produces the magnetic field rotation across the RDs, maintains zero current elsewhere and enforces quasi-neutrality in the region between the SSs. These roles will be discussed in more detail in following subsections. In addition,

we show the parallel phase spaces $y - V_{i\|}$, $y - V_{e\|}$ ($V_\| = \mathbf{V} \cdot \mathbf{B}/B$) in Fig. 2.7(c), (e) and the zoom-in of the region between the SSs in (d), (f). Note that in these figures positive $V_\|$ corresponds to positive V_y, and *vice versa*.

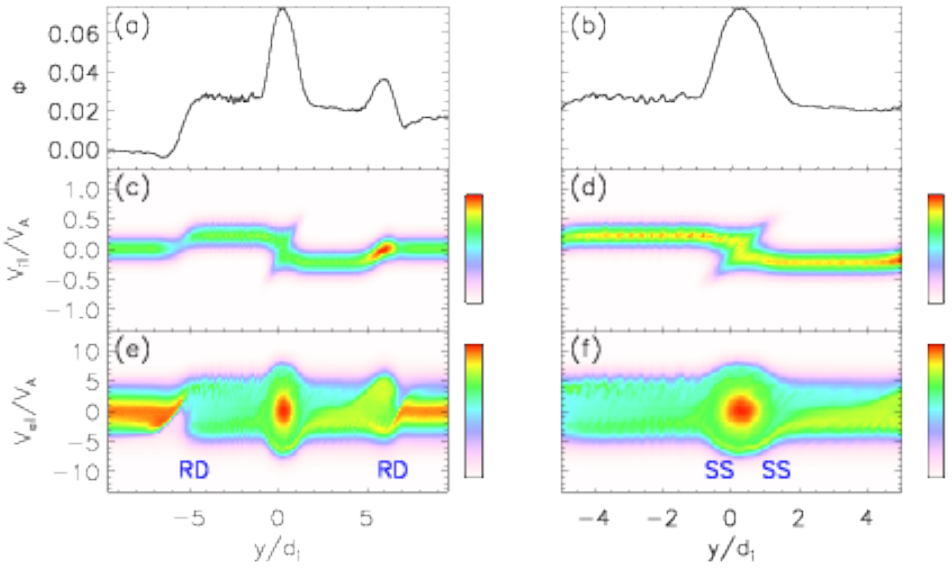

Figure 2.7: On the left, from top to bottom, the profile of parallel electric potential ϕ (a), ion phase space $y - V_{i\|}$ (c) and electron phase space $y - V_{e\|}$ (e) across the whole exhaust. On the right, the same quantities (b) (d) (f) zooming in on the region between the SSs.

Before discussing in more detail the structure of the RDs and SSs we address the role of current-driven instabilities in the low β environment considered here. Since the z component of the magnetic field is the dominant component in the reconnection exhaust between the two RDs (the x component is nearly zero while B_y remains small (see Fig. 2.5(a)), a long enough z dimension in the simulations can capture magnetic field aligned streaming instabilities. The length of the z dimension

in our 2D Riemann simulations is chosen to capture electron-electron, electron-ion or ion-ion streaming instabilities. The characteristic scale lengths are u_b/ω_{pe} for electron-electron and electron-ion instabilites, and V_{eth}/ω_{pe} for ion-ion instabilities, where u_b is the relative velocity between two beams and V_{eth} is the electron thermal speed [56, 57]. In Fig. 2.8, we show the parallel electric field $E_\parallel = \mathbf{E} \cdot \mathbf{B}/B$ in the $y-z$ plane of the Run 3 simulation listed in Table 2.1. There is evidence for instability at each RD (especially at the left RD), but there is no instability around or downstream of the SSs. We focus on the left RD, which exhibits a stronger instability. The turbulence is produced by the Buneman instability driven by the electron beam supporting the current at the RD. Since the width of the RD in the simulation has a d_i scale, from Ampere's law, the beam speed is on the order of $B_{x,u}c/4\pi ned_i = C_{Ax,u}$, the Alfvén speed. So the instability is expected to become weaker with higher mass ratio due to the higher electron thermal speed relative to Alfvén speed. In Fig. 2.9, we compare the instability in the current run (Run 3) with mass ratio 400 to that in Run 4 with mass ratio 100. We see that the instability is significantly weaker in the higher mass ratio simulations. Further, from the electron phase space in Fig. 2.7, we see that the instability does not significantly limit the electron beam at the left RD. Thus, the instabilities do not play a significant role either in the region around the SSs or the RDs. The driver for the instabilities and their impact on the exhaust profile will be discussed in greater detail in the next chapter.

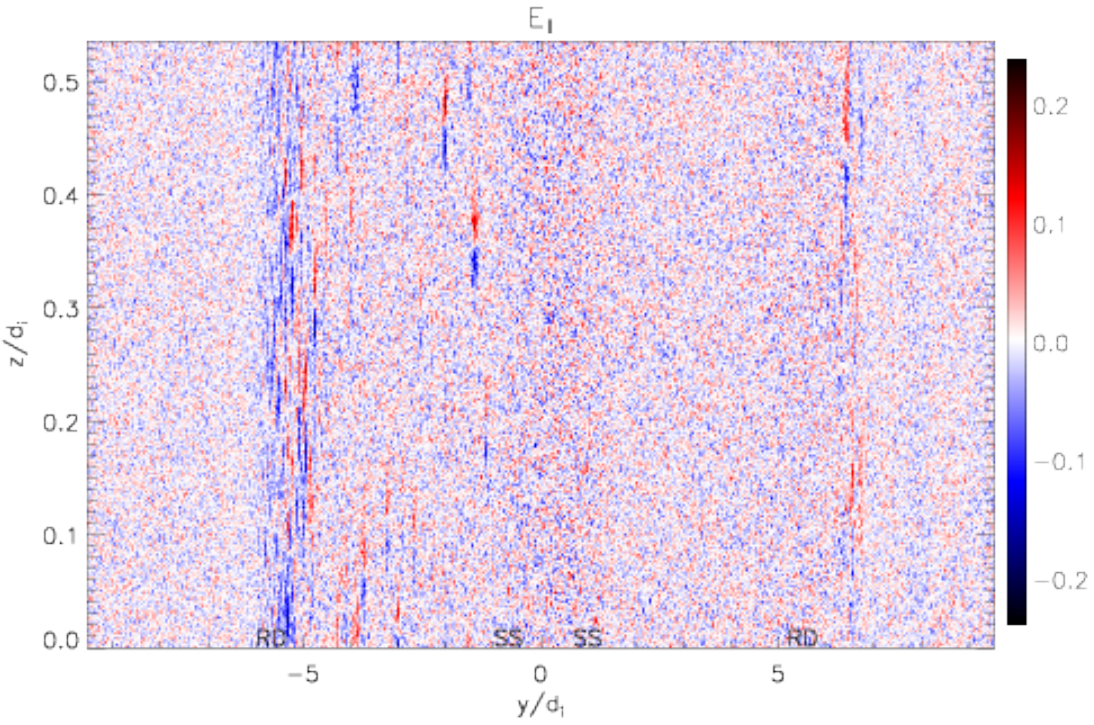

Figure 2.8: Parallel electric field $E_{\parallel}$ from the 2D Riemann simulation (Run 3). Note the different axis scales.

2.3.2 Rotational discontinuity (RD)

Across an RD ions undergo a jump in velocity that can be calculated from the MHD model [2]. In the limit of low upstream β,

$$\begin{aligned} V_{x,d} &= s\frac{B_{x,d} - B_{x,u}}{\sqrt{4\pi n_0 m_i}} \\ V_{z,d} &= s\frac{B_{z,d} - B_{z,u}}{\sqrt{4\pi n_0 m_i}} \end{aligned} \tag{2.1}$$

where the subscripts u, d designate upstream and downstream of the RD and $s = sgn(V_{yu}B_{yu})$, all evaluated in the frame of the RD. Equation (2.1) agrees well with simulations carried out with sufficiently low upstream β. It can not only predict

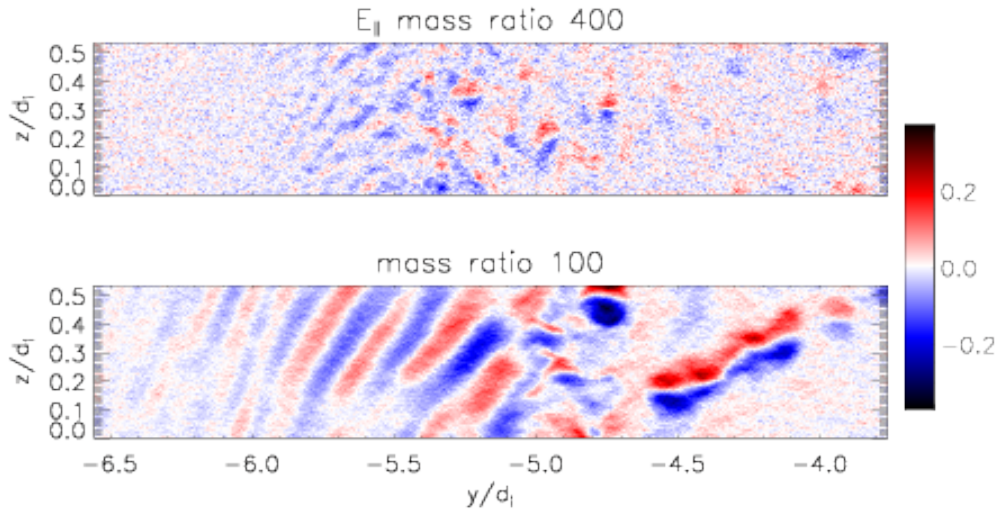

Figure 2.9: Parallel electric field $E_{\parallel}$ of the left RD region from two 2D Riemann simulations Run 3 (top) and Run 4 (bottom) at the same time. The two figures have the same spatial and color scales.

the total jump across the RD but also the continuous transition across the RD, if the downstream magnetic field is treated as a continuous function. As shown in Fig. 2.6(a), the purple dashed lines are consistent with the velocity profiles. The ion velocities in x and z directions are driven by magnetic tension in x and z. Equation (2.1) indicates that V_z downstream of the RDs has opposite signs on either side of the midplane as seen in Fig. 2.6(a). This leads to two ion beams traveling towards the center along the magnetic field with $V_0 \approx |V_{z,d}|$, since B_z is the dominant magnetic field component between the two RDs. These two beams counterstream and give rise to the two SSs. Note that in Fig. 2.6(a), V_x is symmetric because B_x and s are anti-symmetric. V_z is anti-symmetric because B_z is symmetric while s is

anti-symmetric.

While the ion motion across the RDs is controlled by magnetic tension, the electrons are controlled by the localized parallel potentials at the RDs. As a result of these potentials, the electron distributions carry a localized parallel current at the RDs to support the magnetic field rotation while maintaining zero current elsewhere. This leads to partial electron confinement within the exhaust. We demonstrate this in Fig. 2.10. We show the phase space $y - V_{e\|}$ of the RD regions on the left and right of the exhaust and overplot the contours of parallel mechanical energy evaluated in the frame of the RD at the outer edge of exhaust. The mechanical energy is obtained by calculating $\frac{1}{2}m_e(V_{e\|} - V_{ramp\|})^2 - e\phi$, where ϕ is calculated as in Fig. 2.7(a) and $V_{ramp\|}$ is the effective speed of the potential ramp along the magnetic field seen by the electrons. So $V_{ramp\|} = V_{ramp,y}B/B_y$ where $V_{ramp,y}$ is the ramp speed relative to the $\mathbf{E} \times \mathbf{B}$ drift in y direction at the ramp. We measure $V_{ramp\|}$ to be -2.0 for the left RD and 2.2 for the right RD. In Fig. 2.10 we see that the electrons mostly follow the stream lines, suggesting the potential is controlling the electron motion. In this phase space electrons with positive (negative) $V_{e\|}$ at the left (right) RD are streaming toward the midplane of the exhaust. As electrons enter the left RD from upstream (positive $V_{e\|}$) a small potential dip reflects some of the low-velocity electrons. The dominant potential (see Fig. 2.7(a)) then accelerates the incoming electrons across the RD, driving a localized current at the RD that supports the magnetic field jump. Most of the electrons moving toward the left RD from within the exhaust are reflected by the potential at the RD and therefore are effectively confined within the exhaust. At the right RD, the downstream outgoing

electrons are first accelerated towards upstream and then decelerated to produce the localized current that supports the magnetic field jump at the RD (see the potential in Fig. 2.7(a)). Some of these electrons leak out of the exhaust, while some are reflected back towards the midplane. Similarly, some of the incoming electrons are accelerated into the exhaust and then decelerated. Other incoming electrons (negative $V_{e\|}$) are reflected back upstream by a small potential dip. Comparing both RDs, more of the downstream electrons leak across the right RD to the upstream than across the left RD. Thus, a higher fraction of electrons are confined by the RD where the electric field driving the current at the RD acts as a confining electric field. The electron confinement at either side helps to maintain zero current upstream. In the regions between the RD and the SS on either side, as in Fig. 2.7(e), there are electrons from the RD and electrons that have escaped from the region between the two SSs. The multiple electron populations between the RD and the SS contribute to a somewhat higher electron temperature than upstream, which is seen at the shoulders in Fig. 2.5(b). There is no counterpart to these shoulders in the MHD model.

Electron confinement at the edge of the exhaust was also observed in simulations reported by Egedal et al. [5, 41]. Their reconnection simulations were in the low-β, anti-parallel regime. They found almost complete electron confinement on both sides of the exhaust in the region just downstream of the x-line. This was a consequence of a large potential which was driven by the magnetic expansion and ion demagnetization near the x-line. This mechanism, however, is not active far downstream of the x-line where ions are magnetized. Further, in guide field recon-

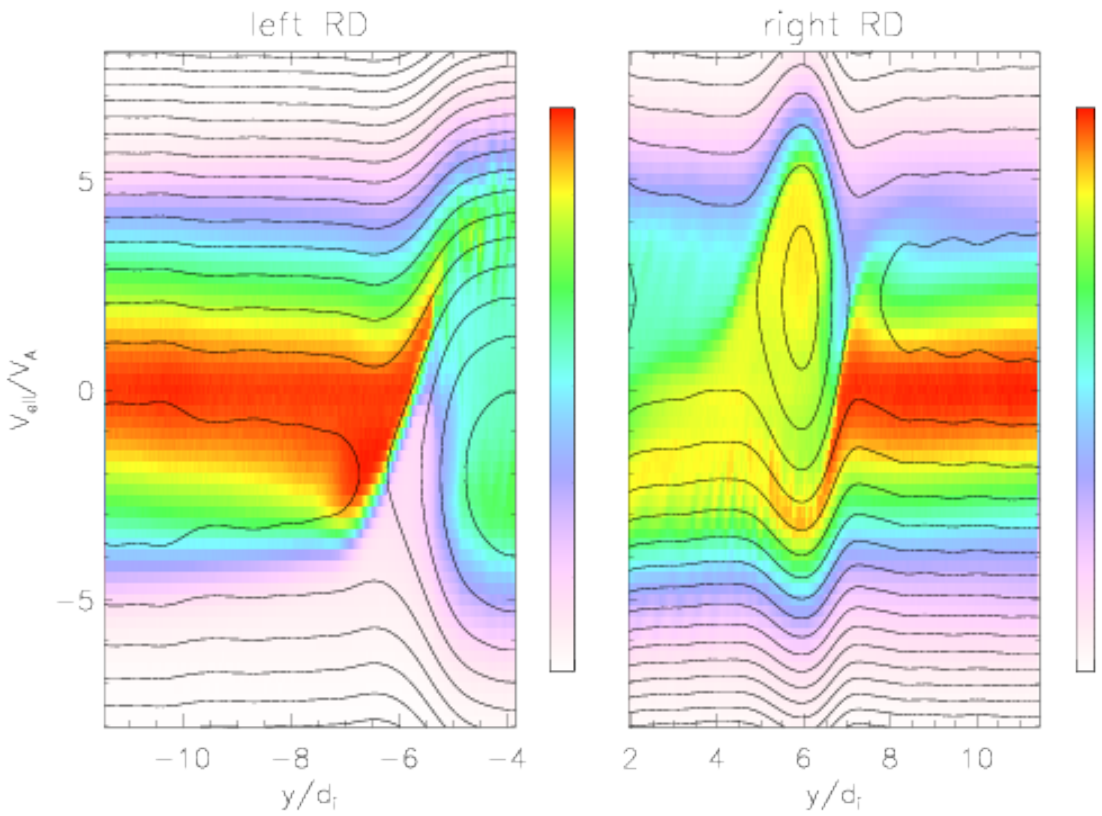

Figure 2.10: The phase space $y - V_{e\|}$ of the regions around the RDs on the left and right of the exhaust with the contours of parallel mechanical energy evaluated using the potential at this time in the frame of the RD potential ramp at the outer edge to show the approximate phase space stream lines of electrons under the potential.

nection magnetic expansion is suppressed. As a consequence, we do not see such a large confinement potential develop, especially at the right RD.

2.3.3 Slow Shock (SS)

In the region between the SSs, the dynamics of both ions and electrons are controlled by the parallel potential. As shown in Fig. 2.6(b), upstream of the shock both ions and electrons have the same density, which is close to the ambient density n_0 upstream of the RDs. In Fig. 2.7(d), ions moving from upstream to downstream across the SSs are decelerated with a small fraction reflected. Some faster ions reach

the SS on the other side of the exhaust and are accelerated into the region upstream of the SS. The counterstreaming ion beams around and between the SSs increase the effective ion temperature although the distributions retain beam-like features.

In contrast with the ions, the electrons are accelerated downstream across the SSs (Fig. 2.7(f)). Since the SSs are moving outward, some lower energy electrons are trapped by the retreating potentials and lose energy over time due to conservation of the second adiabatic invariant as the region between the SSs expands. Other higher energy electrons have high enough energy to go through the potential to escape from the region between the two SSs. The trapped electrons result in the higher electron temperature downstream of the SSs. Since it is the ion beams that are the energy source of the SSs, the electron heating represents the conversion of ion bulk flow energy to the electrons. Note that in the electron phase space shown in Fig. 2.7(f), there is a localized peak near (y=0, $V_{e\|}$=0) on the top of the rest of distributions with the maximum phase space density close to the initial distribution maximum. This is a trapped population left over from the initial formation of the RD and SS. These trapped electrons lose energy as the exhaust expands and become energetically unimportant at late time.

The two SSs are formed by the counterstreaming ion beams produced at the RDs (see Fig. 2.6(a)). In the frame of the exhaust downstream of the RDs the beams propagate along the nearly constant magnetic field (see Fig. 2.5(a)) so the resulting SSs are electrostatic shocks. The charge imbalance driven by the beams produces the jump in the parallel potential across the SSs. If there were no potential, the counterstreaming ion beams would produce an ion density of $2n_0$ in the central

region. In contrast, due to high electron thermal velocity, only half of the electrons from either side would reach the region with counterstreaming ions. The remaining half of the electrons would never reach the region of counterstreaming ions. Thus, in the absence of the potential, the central electron density would be only n_0. The charge imbalance between ions and electrons drives the potential, which modifies the distribution functions of both species and restores quasineutrality. In the low initial β limit of the anisotropic MHD model as is discussed in the Appendix, the speed of the SS along the magnetic field is close to V_0, just like a gas dynamic shock. This speed matches the results of simulations with sufficiently low β. If the inflowing distributions of ions and electrons into the region between the SSs were known, one could use Liouville's theorem to kinetically express the ion and electron distributions at the center downstream of the two SSs as a function of the potential jump across the shock, which would yield their densities. Using quasineutrality one could then equate the densities of ions and electrons to solve for ϕ and use it to determine the central distribution functions, densities and temperatures. Thus, it is quasineutrality that controls the magnitude of the potential and the dynamics of ions and electrons. However, the major difficulty with this method is that the inflowing electron distributions into the SS from the RD are nontrivial (as discussed in the previous subsection). We will further discuss the quasineutrality requirement in the low-β regime in the next section.

2.4 Scaling of heating and energy partition in the low-β regime

2.4.1 Justification of 1D Riemann simulations

To explore the scaling of ion and electron heating in the low-β regime we perform a series of 1D Riemann simulations. By ignoring the z direction, we eliminate the possible development of streaming instabilities such as those seen in Fig. 2.8. However, these instabilities have little effect on the system's development. To demonstrate this we show in Fig. 2.11 a comparison between a 2D Riemann simulation in the y-z plane (Run 3) and a 1D Riemann (Run 5) simulation based on the same parameters. Panels a and b show the phase spaces and panels c and d (black line) show the $T_{e\|}$ profiles. The similarity of the panels suggests that the eliminated instabilities that did develop in the 2D simulation are too weak to have a significant impact on the results. Also we show in panel d (green line) the $T_{e\|}$ profile from Run 13 with a mass ratio 1600 and otherwise the same physical parameters as Run 5 to demonstrate that the results are not sensitive to the mass ratio as long as it is high enough. In addition, we perform a 1D Riemann simulation (Run 14) doubling the domain size in y of Run 5, so that we can double the simulation time from 60 to 120. We show the electron parallel temperature profiles at t=60 and t=120 in Fig. 2.12. We demonstrate that the structures and heating remains the same as the exhaust further expands over time. Hence, in the next section we will use 1D Riemann simulations to scan the low-β regime.

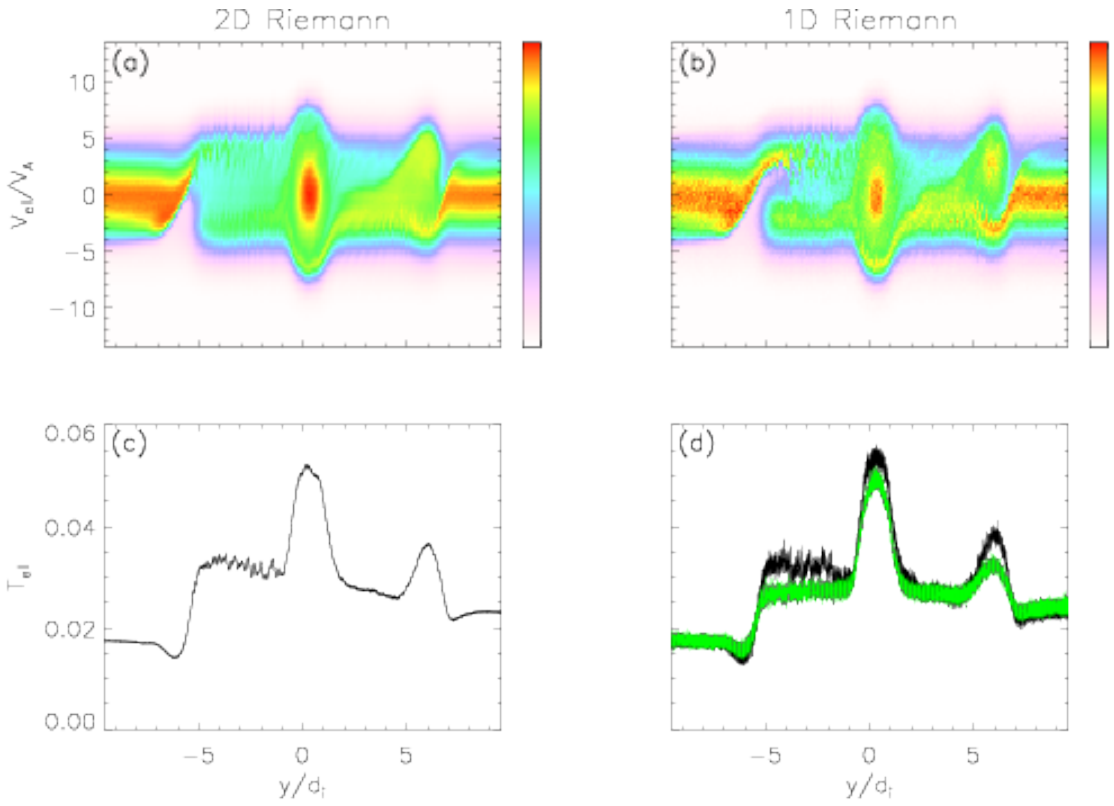

Figure 2.11: Comparing a 2D Riemann simulation and a 1D Riemann simulation. On the left from the 2D Riemann simulation (Run 3), the electron phase space $y - V_{e\parallel}$ (a) and the profile of $T_{e\parallel}$ (c). On the right the corresponding quantities (b) (d) from the 1D Riemann simulation (Run 5). The green line in (d) is the $T_{e\parallel}$ profile from Run 13 with mass ratio 1600.

2.4.2 Scaling of electron and ion heating with the released magnetic energy

Here we present a series of simulations (Runs 5-11) in which the only difference in the initial profiles of the physical quantities are the magnitudes of the upstream magnetic fields. For these runs the electron β varies between 0.1 and 0.0025. For the lower β, the higher mass ratio is needed to ensure that the electron thermal speed exceeds the characteristic ion flow, RD and SS effective speeds along the field, etc. The requirements on the mass ratio will be discussed more in the next subsection.

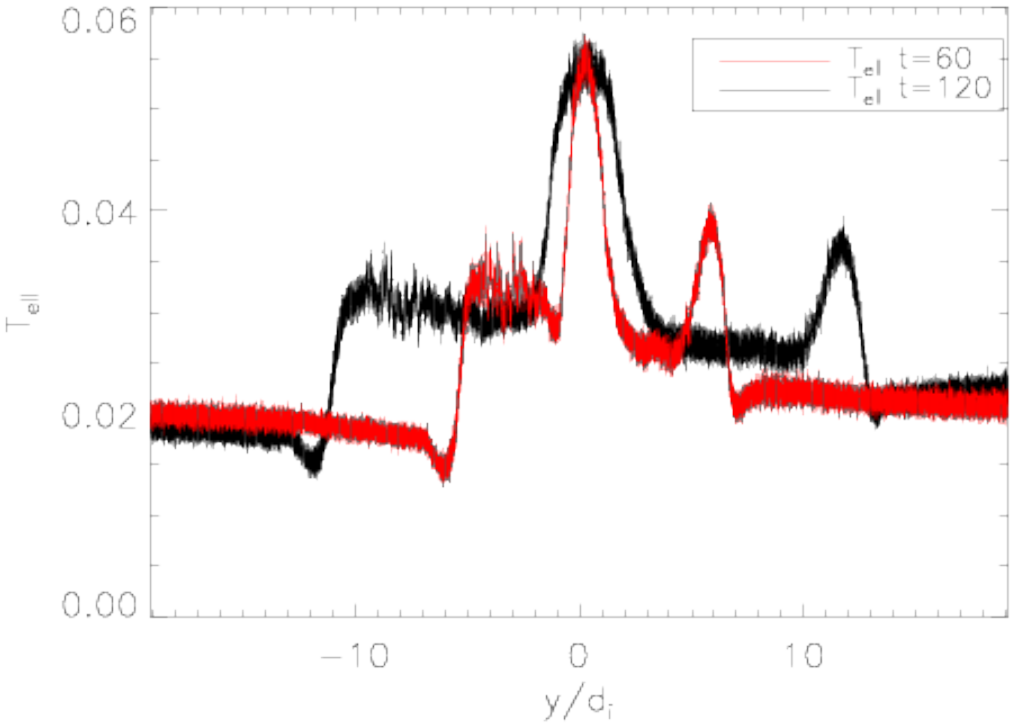

Figure 2.12: The parallel electron temperature profiles of Run 14 at t=60 and t=120.

In Fig. 2.13, we plot the variation of the ion and electron temperature increase averaged over the region between the two SSs. The horizontal axis is the available magnetic energy per particle in the low-β limit $m_i C_{Ax,u}^2/(1+B_{z,u}/B_u)$ derived from anisotropic MHD (see the Appendix).

We see in Fig. 2.13 that the ion heating is proportional to the available magnetic energy per particle in the low β limit as expected, while the electron heating reaches a plateau in the low-β limit. In contrast, previous observational and computational reconnection scaling studies suggest that the electron heating should exhibit a linear scaling [39, 46]. However, these previous studies only focused on the β of order unity regime and therefore did not reach low enough β to see the saturation

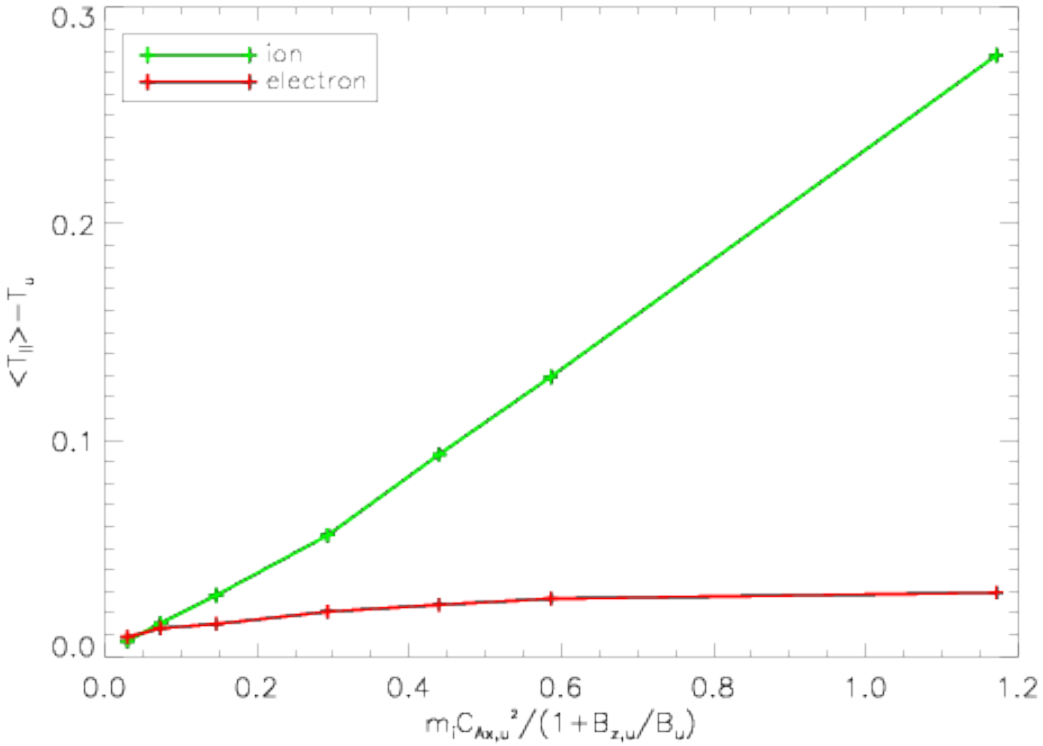

Figure 2.13: The scaling of parallel heating of ions and electrons as a function of available magnetic energy per particle using data from Runs 5-10

of the electron heating. We find one simulation (number 302) in Shay's paper [39] with both initial ion to electron temperature ratio and guide field to reconnecting field ratio equal to one that can be compared with one of our simulations. We confirm that our highest β run (Run 6) produces comparable electron heating to Shay's simulation if we renormalize our run's available magnetic energy per particle to be the same as Shay's run and we calculate the heating averaged over the whole exhaust as Shay did. Therefore, the Riemann simulation results here are consistent with the previous results at higher β. The physical reason for the saturation of electron heating with available magnetic energy is discussed in the next subsection. The consequence is that the ion heating dominates over electron heating in the limit

of low upstream β.

The SS potential can be evaluated by integrating the electron parallel momentum equation across the SS neglecting the inertia term [40],

$$e\Delta\phi = \Delta T_{e\|} + \int ds T_{e\|} \nabla_\| \ln(n) + \int ds (T_{e\|} - T_{e\perp}) \nabla_\| \ln(B), \tag{2.2}$$

with ds the distance along the local magnetic field. The third term on the right can be neglected because the magnetic field is nearly constant across the SS. The potential therefore scales like the electron temperature. Since this is small in the low β limit, the potential is insufficient to significantly alter the velocity of the ions as they cross the SS. The consequence is that ion reflection by the shock potential does not take place, which eliminates the reflected ion beams upstream of the slow shock that play such an important role in high Mach number parallel shocks. Downstream of the SS the ions remain as distinct counterstreaming beams with essentially no mixing. Although the counterstreaming ion beams have significant free energy, the ion-ion two stream instability along the field lines is stable since the electron temperature is low with the consequence that the ion beam speed is higher than the sound speed $\sqrt{T_{e\|}/m_i}$ [57]. As a crosscheck we carried out a 2D test simulation with uniform magnetic fields and parallel counterstreaming ion beams with speed higher than sound speed. We did not observe any instabilities develop to release the energy associated with the counterstreaming ion beams. This result is consistent with Fujita et al. [57].

2.4.3 The saturation of electron heating at low β

Here we discuss the physics behind the saturation of electron heating in the low β regime. The electron parallel temperature increase across the RD in our simulations is small because the electron thermal speeds are much higher than the streaming velocities at the RDs required to form the current needed to switch-off B_x. As the electrons downstream of the RD cross the SS, the electrons gain energy because of the high potential between the SSs. Electrons below a critical speed V_{trap} in the lab frame will get trapped between the SSs, while those above it will free stream across both SSs to the other side of the exhaust. We evaluate V_{trap} in the following. We first point out that an electron with this critical velocity upstream of the first SS will, after passing through both SSs, reach zero velocity in the frame of the second. We trace an electron with zero velocity just outside of the second SS backwards in time. Before crossing the second SS this electron has a velocity $V_\phi = \sqrt{2\phi/m_e}$ in the frame of the SS. Switching to the frame of the first potential, its parallel velocity is $V_\phi + 2V_s$ where V_s is the effective speed of the SS along the magnetic field in the lab frame. In this frame before crossing the first potential, the speed is $\sqrt{(V_\phi + 2V_s)^2 - V_\phi^2} = 2\sqrt{V_s V_\phi + V_s^2}$. Now changing back to the lab frame, we obtain the critical velocity $V_{trap} = 2\sqrt{V_s V_\phi + V_s^2} - V_s$. The trapped electrons then undergo adiabatic deceleration in the expanding trap. We demonstrate this in Fig. 2.14 using a test particle trajectory in the phase space $y - V_{e\|}$. Here we have applied the time dependent background profiles of magnetic fields and smoothed parallel electric potentials from Run 11. The potential profile is obtained from

equation (2.2), which is close to that from directly integrating parallel electric fields as in Fig. 2.7(a). The particle starts at the diamond point and moves from black to red color over time, decelerating towards zero velocity.

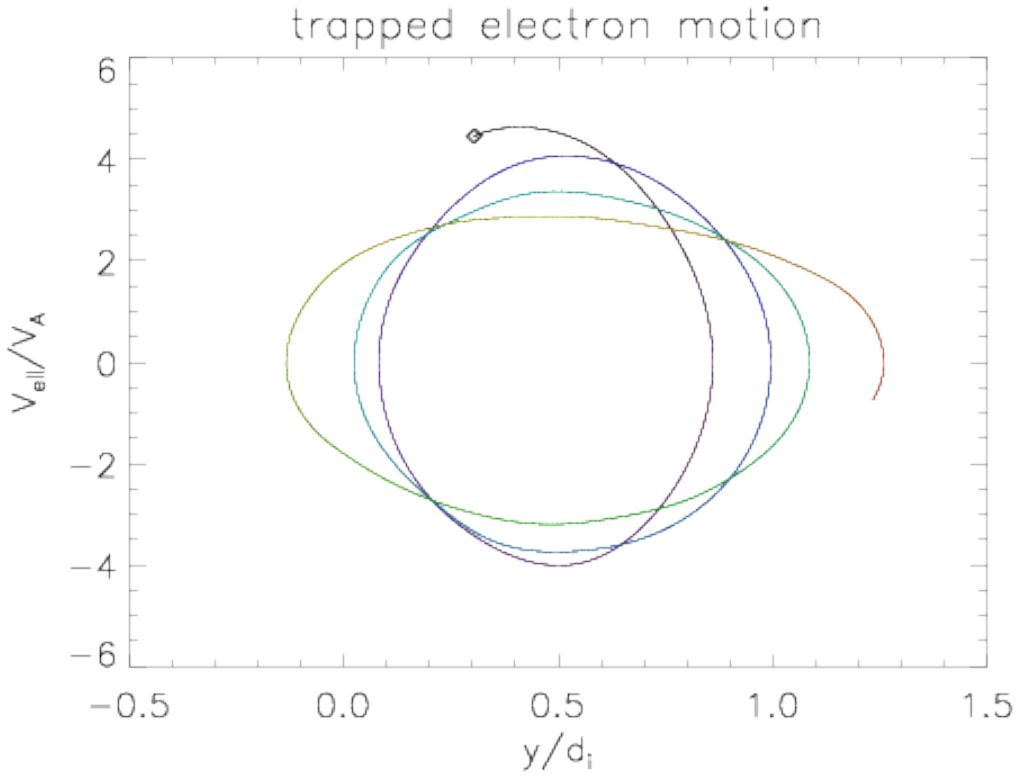

Figure 2.14: A test particle trajectory in $y - V_{e\|}$ phase space using the smoothed magnetic fields and parallel electric potential from Run 11. The trajectory begins at the diamond and changes color from black to red during the particle motion.

From charge neutrality the flux of ions and electrons that remains between the SSs must be equal. In the low β limit, the upstream ion is an incoming beam with speed $2V_s$, so the incoming ion flux is $2n_0V_s$. All of these ions remain between the two SSs. The trapped electrons make up the dominant component of the downstream electrons since the untrapped electrons transit out of the region between the SSs very quickly. Thus, the incoming flux of electrons that will be trapped must match the total incoming flux of ions. We take the upstream thermal speed $V_{eth,u} \gg V_s$

(so β can not be too low) and $V_\phi \gg V_s$ so V_{trap} simplifies to $2\sqrt{V_s V_\phi}$. The upstream electrons with velocities between v=0 and $2\sqrt{V_s V_\phi}$ will be trapped. Taking $V_{eth,u} \gg V_{trap}$, the fraction of trapped electrons is $V_{trap}/V_{et,u}$. The electron flux is then given by $n_0 V_{trap}^2/2V_{eth,u}$. Equating the incoming fluxes of the two species, we have

$$n_0 \frac{V_{trap}^2}{2V_{eth,u}} \sim 2n_0 V_s \tag{2.3}$$

to obtain $V_\phi \sim V_{eth,u}$ or $e\phi \sim T_{e,u}$. Therefore, $T_{e,d} \sim e\phi \sim T_{e,u}$. Thus, the electron heating can not be very strong even with large available magnetic energy per particle and the electron heating reaches a plateau as shown in Fig. 2.13. Physically, this is because the electron heating is limited by the amplitude of the potential across the SSs. A very large potential does not develop because it would trap too many electrons compared with the modest increase in ion density (a factor of two) and so charge neutrality would be violated.

The conditions used above, $V_{eth,u} \sim V_\phi \gg V_s$, are satisfied in our simulations as long as the ion-to-electron mass ratio is sufficiently large.

2.4.4 Partitioning of the ion energy gain

Magnetic energy flows into the exhaust and is converted into different forms of energy. As expected from the dominance of the ion temperature in Fig. 2.13, in the low-β limit the ion thermal energy dominates the electron thermal energy. In this limit, the electron thermal energy upstream and downstream can be neglected. The ion energy gain across the exhaust can be calculated using the anisotropic

MHD solution in the Appendix. The available magnetic energy per particle was calculated previously to be $m_i C_{Ax,u}^2/(1+B_{z,u}/B_u)$. The released magnetic energy partitions into three distinct fractions: $(B_u+B_{z,u})/(2B_u)$ for ion bulk flow energy associated with V_{ix}; $(B_u-B_{z,u})(2B_{z,u}-B_u)/(2B_u^2)$ for ion bulk flow energy in V_{iz}; and $(B_u-B_{z,u})^2/B_u^2$ for ion thermal energy. The fractions total to unity. They can be tested by the same set of simulations used in Fig. 2.13. In the exhaust, we calculate the ratio of these components of the ion energy (normalized by the number of ions) to the available magnetic energy per particle $m_i C_{Ax,u}^2/(1+B_{z,u}/B_u)$ and we plot them as a function of $m_i C_{Ax,u}^2/(1+B_{z,u}/B_u)$ in Fig. 2.15. The summation of the fraction of all forms is close to unity at low-β, suggesting that our prediction of the available magnetic energy per particle is correct. Each line approaches a constant and agrees reasonably well with the corresponding predicted partition by anisotropic MHD in the low initial β limit plotted in red.

2.5 Conclusion

In this chapter we report the results of low-β guide field particle-in-cell Riemann simulations with high ion-electron mass ratio to explore the particle heating in reconnection outflows far downstream from the x-line. Comparison with conventional reconnection simulations shows that Riemann simulations can produce comparable results when the simulation parameters overlap. Thus, Riemann simulations are good proxies of reconnection simulations and can be useful to explore the low-β regime with more realistic parameters than is possible with full 2D recon-

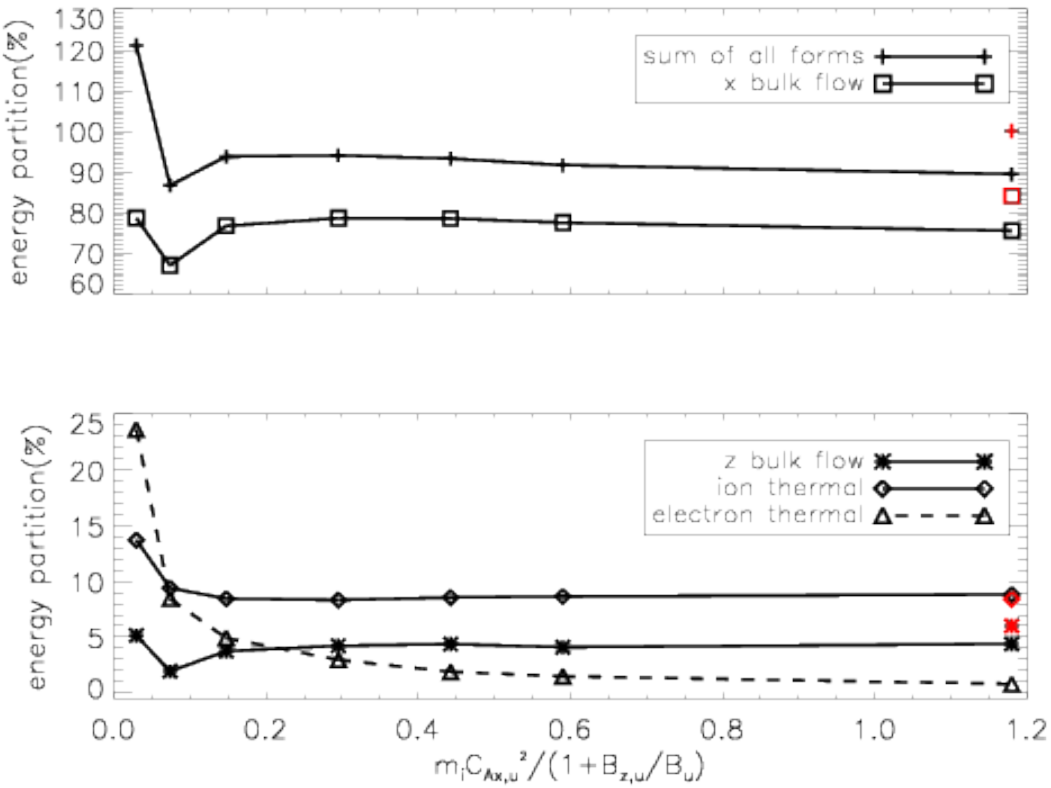

Figure 2.15: Energy partition into different forms of kinetic energy as a function of available magnetic energy per particle. The corresponding predicted partition by anisotropic MHD in the low initial β limit is plotted in red

nection simulations.

The results of Riemann simulations in the low-β regime show that the RDs and SSs associated with reconnection clearly separate from one another, steadily moving outwards from the exhaust midplane. The steady expansion of the exhaust, as long as the domain is large enough, should continue without bound, suggesting that particle heating in the exhausts can extend to macroscopic scales in the corona. There is ion and electron heating between two SSs and electron heating between the RD and SS. The latter produces shoulders in the electron temperature profile that extend across the entire exhaust. The heating mechanisms downstream of the SSs differ from those between the RD and SS. Ions are accelerated by the RD magnetic

field tension and gain bulk flow energy along the x direction (the reconnection exhaust) and in the out-of-plane z direction. Electrons are controlled by the electric potential that forms to produce the localized parallel current to support the magnetic rotation at the RDs and to maintain zero current elsewhere. These potentials partially confine electrons within the exhaust. The two RDs, however, have different confinement characteristics. A higher fraction of electrons are confined by the RD where the electric field driving the current at the RD acts in the same direction as a confining electric field. The ion beams produced at the RDs counterstream across the midplane of the exhaust and create a region of high density (a factor of two above the upstream density) that defines the domain between the SSs. The increase of the ion density leads to a region of high potential between the SSs to confine downstream electrons to maintain charge neutrality. The potential accelerates electrons from upstream of the SSs towards downstream and traps a fraction of them, modestly increasing the downstream electron temperature.

The heating of ions and electrons as a function of available magnetic energy per particle reveals distinct differences between the two species. The ion heating exhibits a roughly linear scaling with available magnetic energy while the electron heating reaches a plateau in the low-β limit. The consequence is that the electron energy increment is only of the same order as the upstream temperature. This is in contrast to the linear scaling for both ions and electrons that would be expected if the heating were simply proportional to the available magnetic energy per particle [46, 47]. The special scaling for electrons originates from the quasineutrality requirement, which prohibits strong electron heating even with large available magnetic energy per

particle. As a result of this scaling, ion heating dominates over electron heating in the low-β limit and the energy partition reduces to an anisotropic MHD prediction with electron energy gain neglected.

Rowan et al. [58] have also investigated guide field reconnection heating and energy partition with realistic mass ratio and low β. They concluded that electrons rather than ions gained most of the released energy in the strong guide field limit. However, they explored the trans-relativistic regime with magnetization $\sigma = B^2/4\pi n m_i c^2 \sim 0.1$. This translates to an electron Alfvén speed close to c. Around the x-line and along magnetic separatrices the electron velocity approaches the electron Alfvén speed so electrons can approach relativistic velocities in a single x-line encounter. In the non-relativistic regime under consideration here, in which most electrons bypass the x-line and enter the exhaust downstream, the electrons gain negligible energy in a single passage through the exhaust. As a consequence, it is the ions rather than electrons that gain significant energy in a single interaction with the rotational discontinuity that bounds the reconnection exhaust. The ions therefore gain the most energy in the non-relativistic limit.

The fundamental physics revealed in this study has broad implications to the inner heliosphere and the corona where reconnection plays a role in magnetic energy conversion. This study specifically raises questions about how electrons gain significant energy in the single x-line model of reconnection-driven flare energy release. With the electron energy gain controlled by potentials in our picture, neither very energetic electron nor very strong electron heating can take place in single x-line reconnection exhausts. The conventional picture of strong electron heating at the

slow shocks produced during reconnection [4, 59] therefore fails. Further, the generation of an energetic electron powerlaw tail up to energies of the order of an MeV as observed in large solar flares [33], is also not possible in a single exhaust. This study suggests that other mechanisms are required to explain electron energy gain in solar flares, such as multiple x-line reconnection [45, 60–62].

The heating mechanism we found in this chapter is mostly controlled by laminar physics but the simulations is at most 2D (y-z) and do not fully capture the turbulence in 3D. To make sure about the role of turbulence in this process, we will explore in depth the dynamics of instabilities and turbulence in 2D (x-y) and 3D exhausts in the next chapter.

Chapter 3: Role of Instabilities and Turbulence

3.1 Introduction

Turbulence is another important fundamental phenomena in plasma physics. It can contribute to particle scattering, transport, acceleration, energy dissipation and so on and it could intertwine with reconnection. So it is fundamental to understand the role of turbulence in reconnection, especially in the process of energy conversion.

Here we focus our attention on turbulence in single x-line reconnection rather than multi x-line reconnection. Turbulence is often driven by instabilities. Previous observational and numerical studies have investigated instabilities and turbulence in reconnection near the diffusion region and along the magnetic separatrices that emanate from the magnetic x-line [36,63–68] as well as in the exhaust downstream of the x-line [38,69–72]. They could contribute to anomalous resistivity and viscosity, cause dissipation and scattering and so on. The major region of energy conversion is the reconnection exhaust downstream of the x-line. Recently, Eastwood et al. [71] observed a guide field reconnection exhaust 100 d_i downstream of the x-line with a β of order unity and identified electron holes. Munoz et al. [69] used low-β ($<$0.1) 2D particle-in-cell (PIC) simulations to explore the turbulence present in guide field

reconnection exhausts. However, the simulation domains only extended about 6 d_i downstream of the x-line so the turbulence further downstream remains to be explored. In this chapter, we will also focus on the guide field and low-β regime, which is relevant to the solar corona and the inner heliosphere, where reconnection can drive powerful releases of magnetic energy in solar flares and coronal mass ejections (CMEs).

To study the exhaust, we will again use the Riemann simulations over the inflow direction y. However, to capture kinetic-scale instabilities and turbulence, a small length in the outflow (x) or guide field (z) direction can be kept, resulting in a 2D or 3D Riemann simulations. Previously 2D (x-y) Riemann simulations have been used to model the instabilities and turbulence of the antiparallel reconnection exhausts using either hybrid [50–52] or PIC [53, 54] models.

In the last chapter, we explored the structure of reconnection exhausts in the low-β, strong-guide-field limit [73]. We showed that the exhaust was bounded by RDs with parallel slow-shocks (SSs) forming within the exhaust as expected from the magnetohydrodynamic (MHD) model [2]. However, the SSs in the simulations remained laminar and were not effective in heating either electrons or ions through the usual diffusive shock acceleration mechanism. In this chapter we explore in much greater depth the instabilities and turbulence in low-β guide field reconnection exhausts to firmly establish the laminar nature of reconnection exhausts in this limit. We carry out a 2D reconnection simulation and 2D and 3D Riemann simulations with various mass-ratios.

The organization of the chapter is the following: in Sec. 3.2 we present the

results of simulations of 2D reconnection exhausts, including a discussion of turbulence; in Sec. 3.3 we present the results of 2D Riemann simulations and analyze the associated turbulence; in Sec. 3.4 we present the results of 3D Riemann simulations and show that there are qualitative differences between 2D and 3D simulations and modest versus large mass-ratio simulations; and in Sec. 3.5 we present the conclusions and implications.

3.2 Instabilities and turbulence in 2D reconnection exhausts

In this chapter, we perform simulations using the particle-in-cell code `p3d` [48]. The particles are advanced by the Newton-Lorentz equations of motion and the fields by Maxwell's equations. We apply periodic boundary conditions to all boundaries, so we have two identical reconnection current sheets to achieve the periodic condition in y. However, we only focus on one current sheet in half of the domain. Here magnetic field strengths are normalized to the initial asymptotic field in x direction $B_{\rm x,a}$, densities to the initial asymptotic density n_0, lengths to the ion inertial length $d_i = c/\omega_{pi}$ based on n_0, times to the inverse ion cyclotron frequency Ω_{ci}^{-1}, velocities to the Alfvén speed C_{Ax} based on $B_{\rm x,a}$ and n_0, and temperatures to $m_i C_{Ax}^2$. In this section, we show results from a 2D guide field reconnection simulation (Run 1) with a guide field equal to the reconnecting field ($B_{\rm z,a}$=$B_{\rm x,a}$), which is initialized by a

force free configuration:

$$B_x = B_{\mathrm{x,a}}\ \tanh(y/w_0), \tag{3.1a}$$

$$B_z = \sqrt{(B^2_{\mathrm{x,a}} + B^2_{\mathrm{z,a}} - B^2_x)}, \tag{3.1b}$$

$$n = n_0, \tag{3.1c}$$

Other parameters are shown in Table 3.1. This simulation has an initial total β of 0.1. In this chapter, the number of particles per grid cell (ppg) is 100 in 2D simulations and is 25 in 3D simulations.

Run	m_i/m_e	$B_{x,a}$	$B_{z,a}$	$T_i = T_e$	dims	$L_y \times L_x \times L_z$	c^2	dx	dt	ppg
1	25	1	1	0.05	2	102.4×409.6 × 0	45	0.0125	5.9e-3	100
2	25	1	1	0.05	2	102.4×16×0	45	0.0125	5.9e-3	100
3	25	1	1	0.05	3	32×8×8	45	0.0125	5.9e-3	25
4	100	1	1	0.05	3	32×4×2	180	0.00625	2.95e-3	25

Table 3.1: Simulation parameters

This simulation creates a steady reconnection exhaust extending for more than 100 d_i along the outflow direction as shown in Fig. 3.1. This simulation was also analyzed in Zhang et al. [73] with emphasis on the heating and the overall structure. Here we focus on the instabilities and turbulence. In Fig. 3.1(a), we show the parallel current $J_{\parallel} = \mathbf{J} \cdot \mathbf{B}/B$, which is mostly carried by electrons. We see the two current sheets bounding the exhaust which are the RDs [73]. The core of the exhaust is highly structured with oblique striations in the current. When these striations first develop downstream of the x-line, the source is from the low density RD. Further downstream, the core of the exhaust become more turbulent and this turbulence appears to be disconnected from the RD. In Fig. 3.1(b), we show the parallel electric field $E_{\parallel} = \mathbf{E} \cdot \mathbf{B}/B$, which indicates ongoing instabilities at both RDs. Those at the bottom RD are strong close to the x-line and fade away further downstream. The fluctuations develop at short scale close to the x-line and then clump to larger scales that link to the striations within the exhaust. The nature of these instabilities and turbulence is dicussed in the next section.

3.3 Studies of instabilities and turbulence using 2D Riemann simulations

3.3.1 Riemann simulations to explore reconnection exhausts

To study the current striations and instabilities in the reconnection exhaust in greater detail, we first simplify the configuration by using Riemann simulations. As has been discussed previously [2, 38, 50, 73], Riemann simulations model the

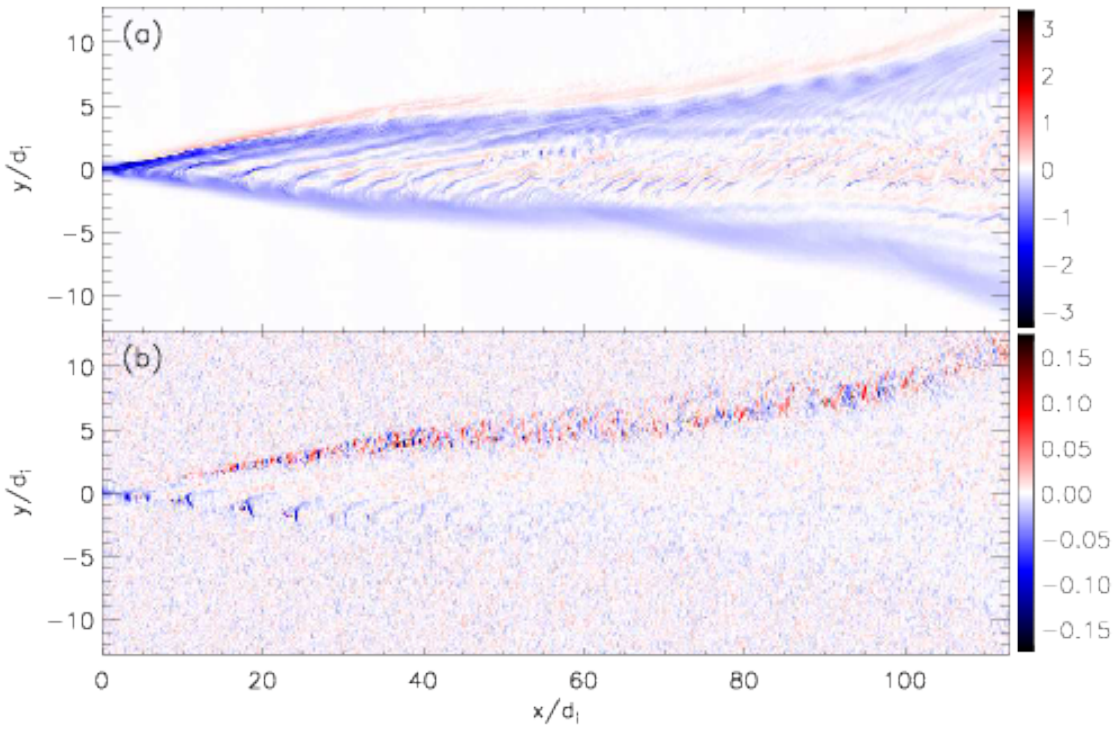

Figure 3.1: $J_{\parallel}$ (a) and $E_{\parallel}$ (b) of a reconnection exhaust in the 2D reconnection simulation Run 1

reconnection exhaust by neglecting the dependence on the outflow direction x. Here since we want to study the structures and instabilities in the x-y plane as in the reconnection simulation, we keep a long enough length in the x dimension to model the striations. Thus, the 2D Riemann simulation is performed in a x-y domain. The parameters (see Run 2 in Table 3.1) and initial profiles are almost the same as Run 1 but there is a small initial magnetic field $B_y = 0.1B_{\mathrm{x,a}}$ added so that the magnetic tension can drive the outflow. In addition, the half width in y of the initial current sheet w_0 is chosen to be close to the half width of the x-line current sheet in Run 1 at the time of Fig. 3.1. The Riemann simulation result at time t is a proxy of the reconnection exhaust region at a distance distance $C_{Ax} * t$ downstream from the

x-line. In the last chapter, we demonstrated that Riemann simulations capture the overall structure of the reconnection exhaust. Here we show that they also capture the development of turbulence and hence can be used as proxies for full simulations to study that turbulence.

We first show the overall 1D profiles (averaged over x) of this 2D Riemann simulation in Fig. 3.2. In panel (a), there are two locations where the magnetic field rotates from the dominant x-z direction to the z direction. These rotations form the RDs that bound the exhaust. In panels (b) and (c), we present the three velocity components of the electrons and ions. The RDs drive the exhaust velocity V_x of both species. The RDs also drive out-of-plane flows V_{iz} that are seen most easily in the ions. These flows are toward the midplane of the exhaust and in the MHD model produce SSs that develop in guide field reconnection. The RDs are supported by a current J_z that produces the magnetic rotation. From Ampere's law the direction of J_z is the same (negative) at both RDs. The electrons have a larger positive V_z than the ions (to create a negative J_z) so the electrons dominate the current at the RD. Since the B_z and B_y are both positive across the domain (panel (a)), the electrons with positive v_z at both RDs are flowing along the field line towards the positive y direction. So the electrons that carry the current at the left RD are at the same time accelerated into the exhaust. The acceleration reduces the local density due to flux continuity and creates a density cavity at the left RD (panel (d)). In contrast, the electrons that carry the current at the right RD are accelerated away from the exhaust, leading to a pileup of the electrons and therefore a density increase. These density variations at the RDs have no counterpart in MHD.

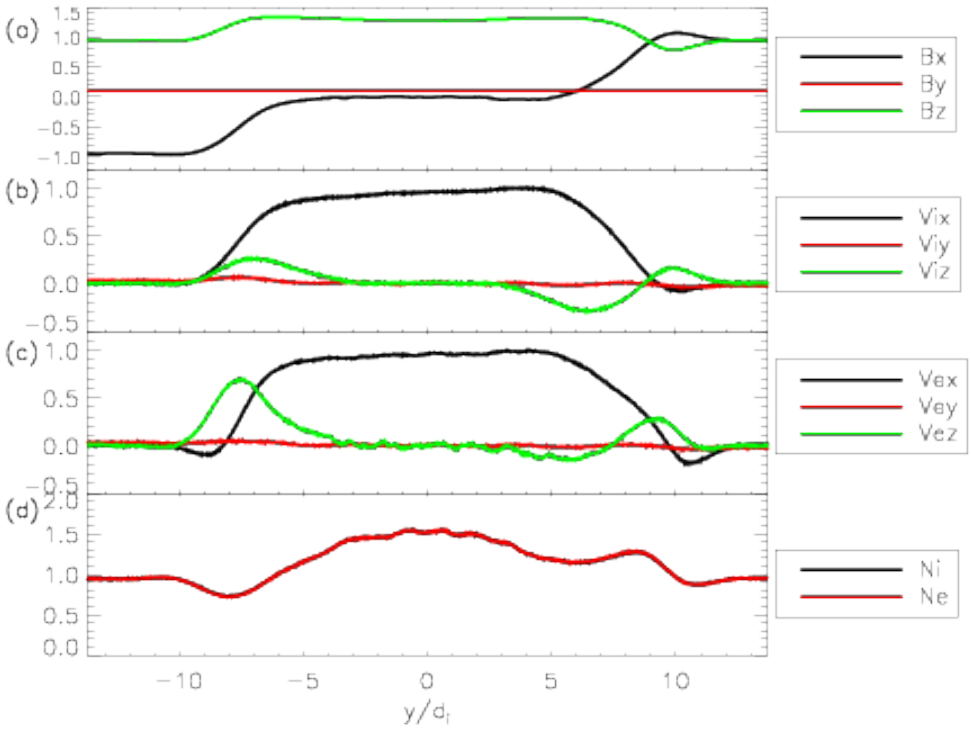

Figure 3.2: The overall 1D profiles (averaged over x) of the 2D Riemann simulation (Run 2). (a) the magnetic fields, (b) ion velocities, (c) electron velocities and (d) ion and electron densities (which nearly overlap).

In Fig. 3.3, we show the results from this 2D Riemann simulation at both early and late time, corresponding to regions of about 25 d_i and 100 d_i downstream of the x-line. Although $L_x = 16$ in this simulation, we only show half the domain with $x \in [0,8]$ to facilitate the comparison to a 3D simulation of a smaller domain shown later in Fig. 3.7. In Fig. 3.3, panels (a) and (b) show $J_\parallel$ and panels (c) and (d) show $E_\parallel$. Comparing to Fig. 3.1, we see that the Riemann simulation captures all the essential features of the instabilities and turbulence we discussed in the 2D reconnection simulation, including the oblique current striations and the structuring of $E_\parallel$. The amplitudes of these fluctuations are also comparable to those in the reconnection simulation. This suggests that the Riemann simulations can be

used to explore the development of turbulence in reconnection exhausts. Therefore, we will use Riemann simulations to explore the nature of these instabilities and the development of turbulence.

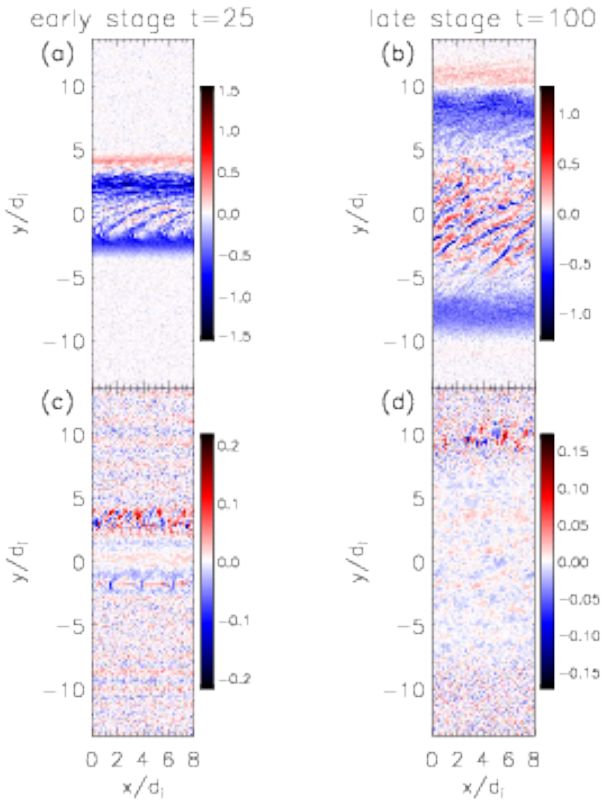

Figure 3.3: (a)(b) $J_{\|}$ and (c)(d) $E_{\|}$ at two times from the 2D Riemann simulation (Run 2).

3.3.2 Studies of instabilities and turbulence

In Fig. 3.4 we show the early evolution of the Riemann simulation to understand the dynamics just downstream of the x-line. Shown are the data from time $t = 5$, 10 and 15. Panels (a)-(c) show $J_{\|}$, and panels (d)-(f) show $E_{\|}$. In panel (d) the instability in the bottom current sheet is still in, or just past, its linear phase. Correspondingly, the current in panel (a) is modified by the instability and

the striations in the current begin to extend from this current sheet into the exhaust. The reason why the current sheet on this side affects the current structures in the exhaust is that the current here is supported by electrons flowing towards the midplane, as discussed in the last subsection. So the structures of the current at this RD convect into the exhaust. Since the exhaust outflow is in the positive x direction relative to the almost stationary upstream plasma (Fig. 3.2(c)), there is a velocity shear that the electrons will experience when they flow from the current sheet into the exhaust. That is why the striations tilt towards the positive x direction. We also show the phase space x-$V_{\parallel}$ in panel (g) which is taken along the green dotted line in panel (d). The ion population is in red and the electron population is in blue. Their maximum phase space densities are normalized to be the same. Since both species are strongly modified by the instabilty, we conclude that the instability is an oblique Buneman instability. This instability can develop in this 2D system with a wave vector k_x because the current has an x component. The wave vector in z can not develop in this 2D x-y simulation. As a cross check, we verified that the dominant k_x was consistent with the prediction for the Buneman instability in Drake et al. [36],

$$k = \delta\omega_{pe}/v_{de}, \tag{3.1}$$

where $\delta^2 = (1 + \sin^2\theta\omega_{pe}^2/\Omega_{ce}^2)^{-1}$. By evaluating the local parameters: electron beam speed $v_{de} = 2$, wave vector direction relative to the field $\cos\theta = 0.3$, density $n = 0.5$, magnetic field $B = 1.4$, we calculate the wavelength along x to be 0.6, which matches that found in the simulation.

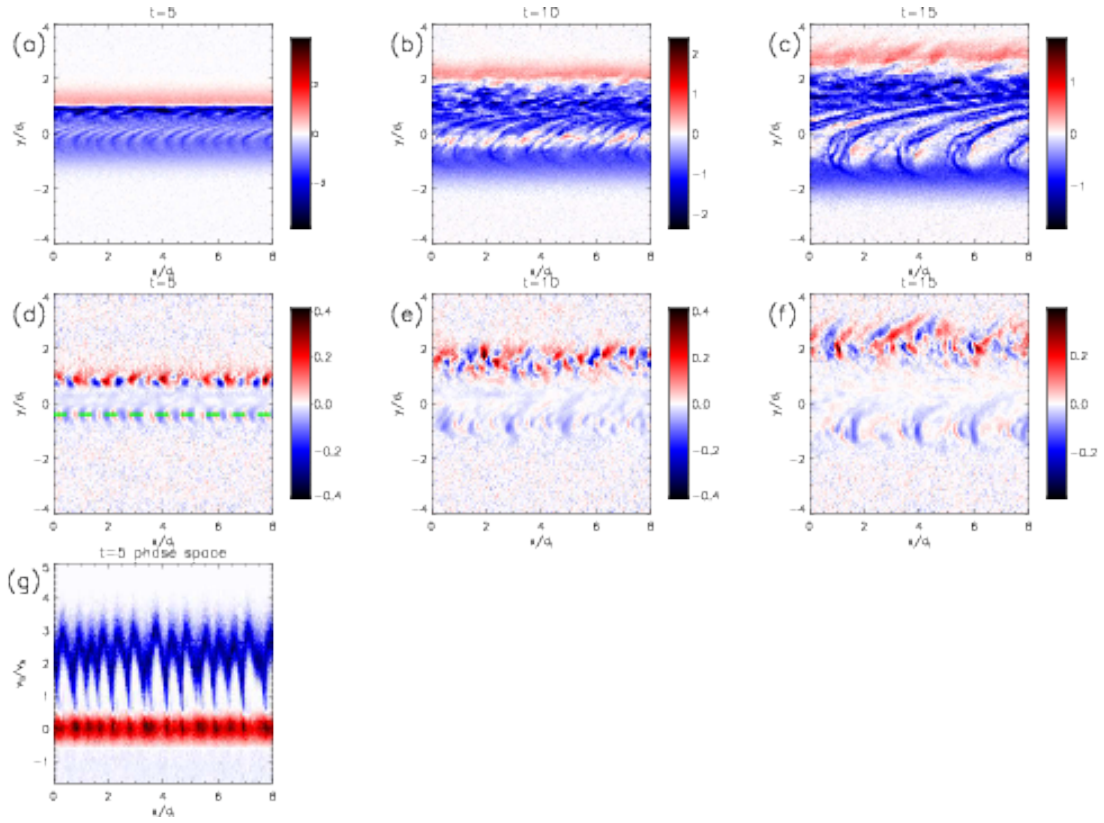

Figure 3.4: The early evolution from Run 2. In (a)-(c) $J_{\|}$ and in (d)-(f) $E_{\|}$. In (g) the phase space x-$V_{\|}$ which is taken along the green dotted line in (d). The ion population in red and the electron population in blue, with their maximum phase space densities normalized to be the same.

In Fig. 3.4(e) and (f), the turbulence at the bottom RD evolves to longer wavelength, forming well-separated, large-scale structures that drive the electron current striations into the core of the exhaust. To understand why the core of the exhaust become more turbulent further downstream and to further clarify how the striations develop in the lower RD, we show in Fig. 3.5 the phase space y-$V_{\|}$ for ions and electrons along a cut in y (at $x = 4$) across the exhaust. We see from the electrons in panel (b) that the instability at the cavity RD (on the left) is weak, so the electron beam flows into the exhaust without dissipation when crossing the RD. After being accelerated into the exhaust, the beam becomes unstable, driving the

turbulence in the exhaust. This instability has $\omega \sim \Omega_{ci}$, $k\rho_i \sim 1$. Since the local magnetic field is dominantly in the out-of-plane direction ($B_x \sim 0$ and $B_z/B_y \sim 13$), this instability's in-plane wave vector is very oblique to the magnetic field ($\cos\theta = 0.054$). To determine the nature of this local instability, we analyse the electrostatic dispersion relation similar to Drummond and Rosenbluth [55] in terms of the plasma dispersion function Z as below:

$$\sum_j \sum_{n=-\infty}^{\infty} \frac{\Gamma_n(k_\perp^2\rho_j^2)}{(k\lambda_{Dj})^2} \left\{ \frac{1}{2} Z' \left(\frac{\omega - k_\parallel u_j - n\Omega_j}{k_\parallel v_j} \right) - \frac{n\Omega_j}{-\omega + k_\parallel u_j + n\Omega_j} \left[1 + \frac{1}{2} Z' \left(\frac{\omega - k_\parallel u_j - n\Omega_j}{k_\parallel v_j} \right) \right] \right\} = 1 \tag{3.2}$$

Here $\Gamma_n(x) = e^{-x} I_n(x)$, $I_n(x)$ is the modified Bessel function of the first kind, $Z'(s)$ is the derivative of the Z function with $Z'(s) = -2(1 + sZ(s))$. The subscript j stands for the different species, v_j is the thermal speed, Ω_j is the cyclotron frequency, $\rho_i = v_j/\Omega_j$ is the Larmor radius, $\lambda_{Dj} = v_j/\omega_{pj}$ is the Debye length where ω_{pj} is the plasma frequency of species j, and u_j is the drift speed. $k_\parallel = k\cos\theta$ is the parallel component of the wave vector and $k_\perp = k\sin\theta \approx k$ is the perpendicular component. We use this dispersion relation to examine a simplified system with three populations: one electron beam (labeled as eb), one lower energy electron population (ec) and one ion population (i), which is analogous to the distributions in Fig. 3.5(b) at around $y = -4$. For simplicity, these populations are assumed to be isotropic Maxwellian distributions and have temperatures close to their parallel temperatures in the simulation. The ion population has density one, temperature 0.05 and speed zero. The electron beam has density 0.3, temperature 0.005 and

speed 2.5. The lower energy electron population has density 0.7, temperature 0.08 and speed $-2.5*0.3/0.7 = -1.07$ to ensure zero current. The total magnetic field is about 1.3. We keep the $|n| \leq 1$ terms in the sum over the Bessel function harmonics and use $k_\parallel v_i \ll \omega \sim \Omega_i$, $\Omega_e \gg k_\parallel v_e$ and $k_\perp^2 \rho_e^2 \ll 1$ to reduce the relation to:

$$\frac{\Gamma_1(k^2\rho_i^2)}{(k\lambda_{Di})^2}\frac{\Omega_i}{\omega-\Omega_i} - \frac{\Gamma_1(k^2\rho_i^2)}{(k\lambda_{Di})^2}\frac{\Omega_i}{\omega+\Omega_i} + \frac{1}{2(k\lambda_{Deb})^2}Z'\left(\frac{\omega-k_\parallel u_{eb}}{k_\parallel v_{eb}}\right) + \frac{1}{2(k\lambda_{Dec})^2}Z'\left(\frac{\omega-k_\parallel u_{ec}}{k_\parallel v_{ec}}\right) - \frac{\omega_{pe}^2}{\Omega_e^2} = 1, \tag{3.3}$$

where ω_{pe} is the electron plasma frequency based on the total electron density. We numerically solve this dispersion relation and plot the solution ω and γ versus k in Fig. 3.6 (a) and (b). The growth rate reaches its maximum at around $k = 1.6$ and slowly decreases at higher k. We have also used a kinetic dispersion relation solver `pdrk` [7] to solve the full electrostatic dispersion relation and we get qualitatively similar results. For the unstable modes around the maximum growth k, the dominant terms in the simplified dispersion relation are the first four terms: two ion terms, one electron beam term and one lower energy electron term. We also tried neglecting the second ion term in the dispersion relation (proportional to $(\omega+\Omega_i)^{-1}$) and find that the result is qualitatively unchanged so the first ion term (the ion cyclotron term proportional to $(\omega-\Omega_i)^{-1}$) and the other two electron terms are dominant. These three terms coupling together suggest that this is an oblique ion cyclotron instability driven by the electron beam. In comparison to the simulation, the k value measured in the simulation is around 5, which is several times larger than the k with the maximum growth rate from this simplified dispersion

relation. This is due to the electromagnetic effects. In fact, we have used `pdrk` to solve the full electromagnetic dispersion relation and show the results in Fig. 3.6 (c) and (d). As seen in panel (d), there is a maximum growth peak at around $k = 5$, in good agreement with the simulation. However, there is also another peak at around $k = 15$, which has also been found either using `pdrk` electrostatic mode or our simplified dispersion relation. However, due to their typically higher saturation amplitudes, longer wavelength modes dominate late time dynamics. We conclude therefore that the striations in the exhaust core are electromagnetic, electron-beam-driven ion cyclotron waves.

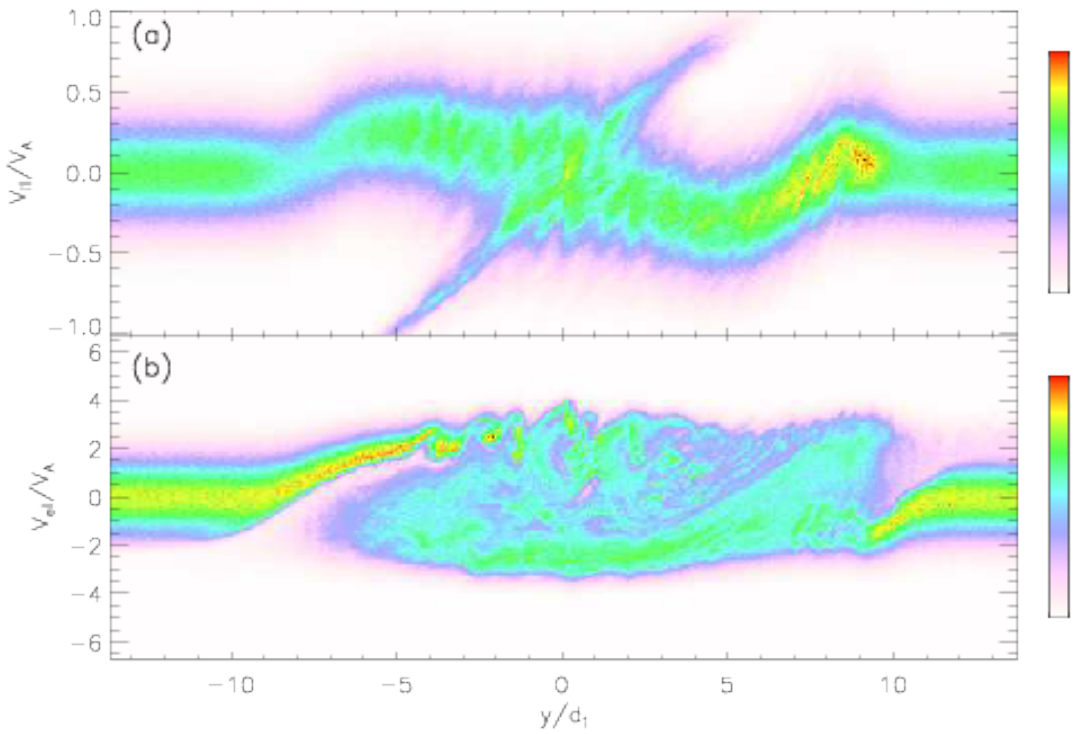

Figure 3.5: The phase space y-$V_{\parallel}$ for ions (a) and electrons (b) along a cut in y across the exhaust of Run 2 at x=4 and t=100.

We have used the 2D Riemann simulation as a proxy to understand the physics

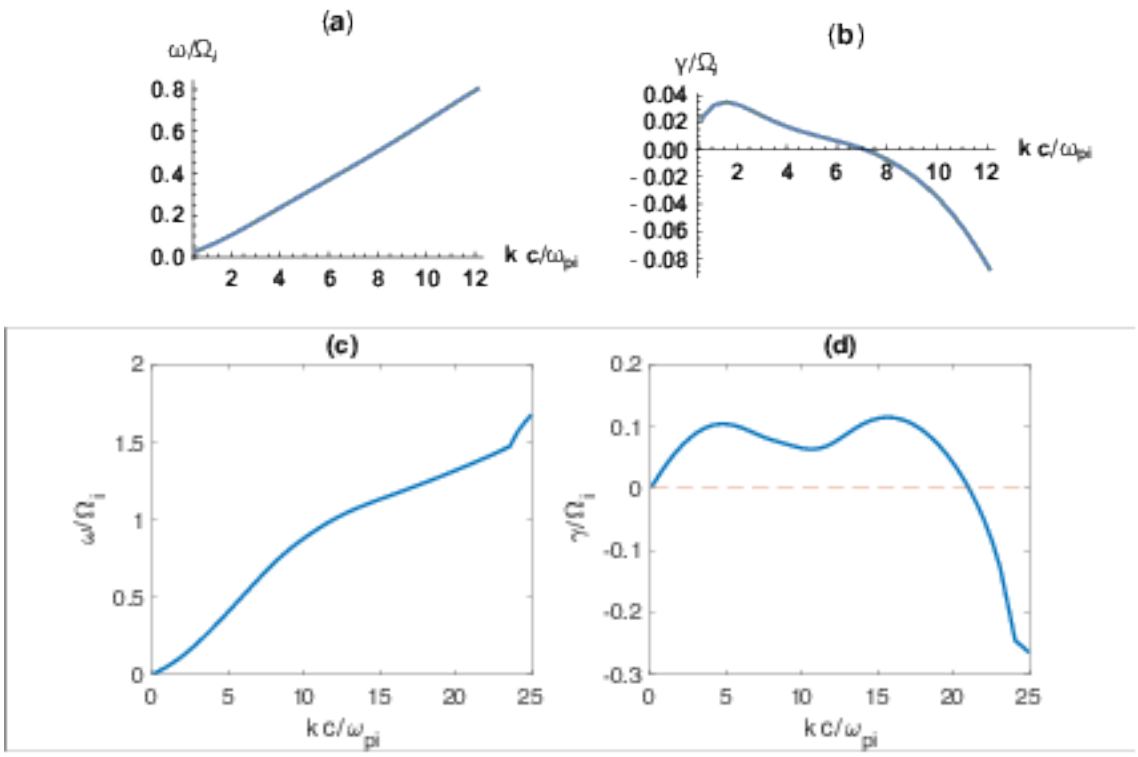

Figure 3.6: The solution ω (a) and γ (b) versus k from the dispersion relation in equation (3.3). In (c) and (d), the solution of the full electromagnetic dispersion relation using the solver `pdrk` [7].

of instabilities and turbulence that develops in the 2D reconnection simulation. However, the 2D limitation forces the instability wave vector in these simulations to be oblique to the magnetic field and thus these simulations may not capture the true nature of the instabilities and turbulence in a real 3D system. Yet a 3D reconnection simulation is too computationally expensive to accommodate an exhaust far downstream of the x-line. We therefore use 3D Riemann simulations to explore the development of turbulence in 3D reconnection exhausts.

3.4 3D Riemann simulations

3.4.1 Comparison to 2D

In Fig. 3.7 we present the results of a 3D Riemann simulation (Run 3) with $L_x = L_z = 8, L_y = 32$ and a reduced number of particles per grid but otherwise the same physical parameters as Run 2. The data is presented in 2D cuts (either x-y or y-z) through the middle of the 3D domain, which is at $z = 4$ and $x = 4$. Due to the lower ppg and higher noise in 3D simulations, the results are slightly smoothed. First, the instabilities exhibit large values of k_z, which could not exist in the 2D simulation. This means that 2D simulations in the x-y plane are not adequate to explore the dynamics of these instabilities. Within the exhaust the magnetic field is dominantly in the z direction so the results of Fig. 3.7 are evidence that wavevectors parallel to the ambient magnetic field are needed to properly describe the turbulence that develops within the exhaust. A surprise from the data in panels (a) and (b) is that the oblique current striations within the exhaust described previously become weak. The data in panels (g) and (h) reveals the growth of strong instabilities with finite k_z at both RDs and within the core of the exhaust. At late time in Fig. 3.7(h) the instability in the bottom (low density) RD does not weaken as it did in 2D (Fig. 3.3(d)). The instability within the exhaust around $y = 5$ in Fig. 3.7(h) was not present in the 2D simulation.

The ion and electron phase spaces $y - V_{\parallel}$ from the Run 3 simulation at $t = 100$ are shown in Fig. 3.8. The cuts are along a line in y across the exhaust at

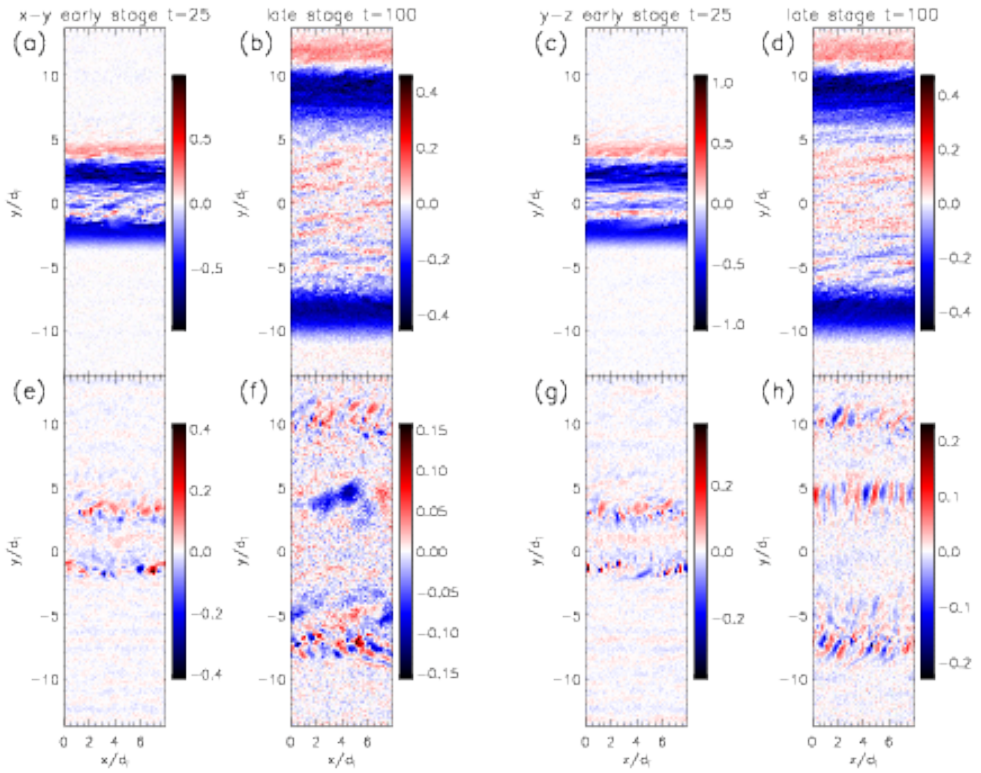

Figure 3.7: The 2D cuts (x-y and y-z) from Run 3 through the middle of the 3D domain at $z = 4$ and $x = 4$, respectively. In (a) and (b) x-y cuts of $J_{\|}$ and in (c) and (d) y-z cuts of $J_{\|}$. In (e) and (f) x-y cuts of $E_{\|}$ and in (g) and (h) y-z cuts of $E_{\|}$.

$x = 4$, $z = 4$. We plot dotted lines in panels (a) and (b) to indicate the y location where the amplitudes of the dominant instabilities peak. The line in panel (a) at $y = 5$ marks the location of the new instability in the core of the exhaust. It is an ion-ion streaming instability that is driven by the counterstreaming ions that are evident in the ion phase space. The instability is also more weakly driven around $y = -5$. This instability will be discussed in depth later in the context of a mass ratio 100 simulation. The two lines in panel (b) are for the instabilities at the RD current sheets. We show the parallel phase space L-$V_{\|}$ along field lines at these two y locations for ions and electrons in panels (c)-(f), where L is the distance

along the magnetic field starting from $x = 0, z = 0$ and moving in the positive z direction. The correlated structuring of the electron and ion phase space along the direction of the magnetic field confirm that the turbulence at these locations is driven by the Buneman instability, which results from the relative drifts of the ions and electrons at both RDs. This strong instability at the low density RD dissipates the current-supporting electron beam more efficiently than in the 2D simulation (compare Fig. 3.5(b) with Fig. 3.8(b)) and prevents it from forming the current striations in the exhaust core.

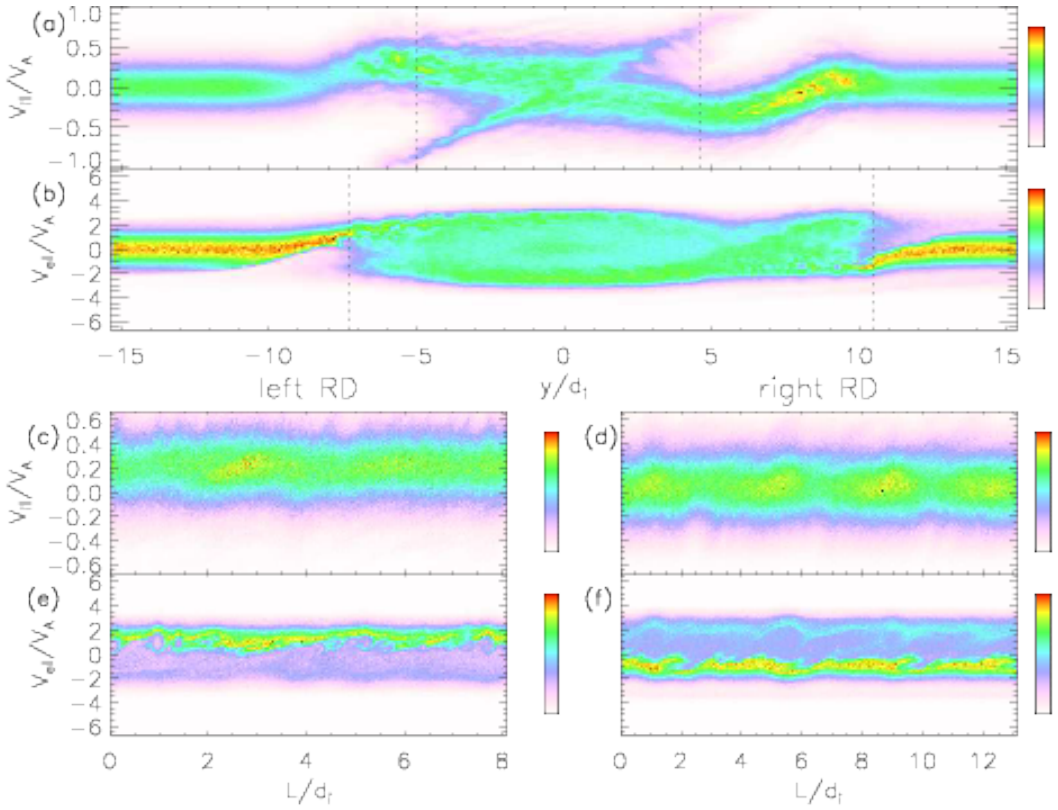

Figure 3.8: In (a) and (b) the ion and electron y-$V_\parallel$ phase space from Run 3 along a line in y across the exhaust at $x = 4$, $z = 4$. Dotted lines in (a) and (b) indicate the y location where instabilities are peaked. The two lines in (a) are for the instability in the core of the exhaust. The other two lines in (b) are for the instabilities at both RD current sheets. The parallel phase space L-$V_\parallel$ along field lines at these two y locations for ions and electrons are shown in (c)-(f), where L is the distance along the field starting from $x = 0, z = 0$ along the positive z direction.

3.4.2 The impact of the mass ratio on the development of turbulence

The results of a 3D Riemann simulation with mass ratio 100 (Run 4) with a domain of $L_x = 4, L_z = 2$ are presented in Fig. 3.9. The other parameters of the simulation are identical to those of Run 3. Thus, the data from the two simulations can be compared to establish the sensitivity of turbulence drive mechanisms to the artificial mass ratio in the simulations. The data is organized in Fig. 3.9 in the same way as in Fig. 3.7, and with the same color bar for each corresponding panel. The x-y and y-z cuts are also through the middle of the 3D domain, which is at $z = 1$ and $x = 2$. Note that we do not respect the image aspect ratio here since the the dimensions x and z would be too short to clearly display the results. The plots displaying $E_{\|}$ reveal that the instabilities develop at shorter wavelength in the mass-ratio 100 run. For Buneman instabilities at the two RDs this is consisent with the expected scaling $k \sim \omega_{pe}/v_{de}$. The turbulence at the RDs is also less well developed in the mass-ratio 100 run, indicating that the turbulence is weaker. For lower electron mass the electron thermal speed increases while the current and therefore the electron drift speed needed to support the RD does not. Thus, the ratio of the electron beam speed to the thermal speed is reduced in the mass-ratio 100 run. This reduces the strength of the Buneman instabilties at the two RDs. In the next section we investigate the ion-ion instability in Run 4.

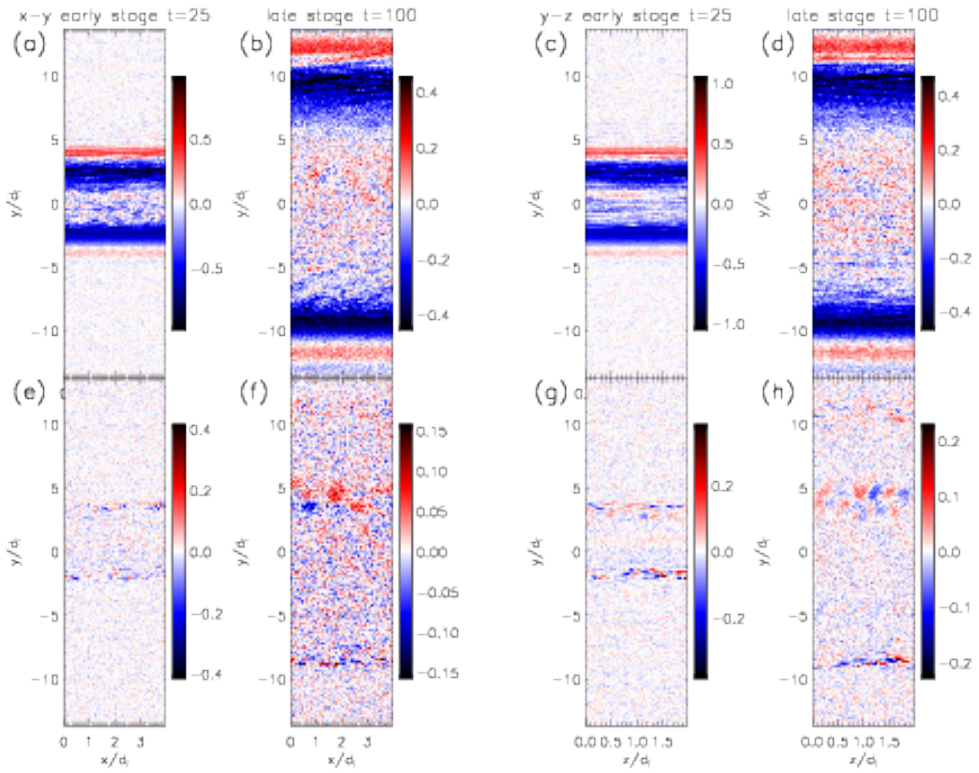

Figure 3.9: The 2D cuts (x-y and y-z) from Run 4 through the middle of the 3D domain at $z = 1$ and $x = 2$, respectively. In (a) and (b) x-y cuts of $J_{\|}$ and in (c) and (d) y-z cuts of $J_{\|}$. In (e) and (f) x-y cuts of $E_{\|}$ and in (g) and (h) y-z cuts of $E_{\|}$. These quantities are organized in the same way as in Fig. 3.7, and with the same color bar for each corresponding panel. Note that we do not respect the image aspect ratio.

3.4.3 Studies of ion-ion instabilities

We now explore the driver of the turbulence seen in the core of the exhaust around $y = 5$ in Figs. 3.9(f) and (h). In Figs. 3.10(a) and (c) we show a blowup of $E_{\|}$ in y-z (at $x = 2$) and x-z (at $y = 4.6$) planes. The white lines show the location of the cuts. This data reveals that the dominant wavevector is along the z direction, which is essentially the magnetic field direction at that location. Also, given that that the magnetic field perturbations there are weak (not shown), this is also an

electrostatic instability. In panels (b) and (d), we show the ion and electron phase spaces z-V_z along the white line in Fig. 3.10(c). The instability weakly perturbs the counterstreaming ion beams and has an even smaller impact on electrons so this appears to be a weak ion-ion streaming instability.

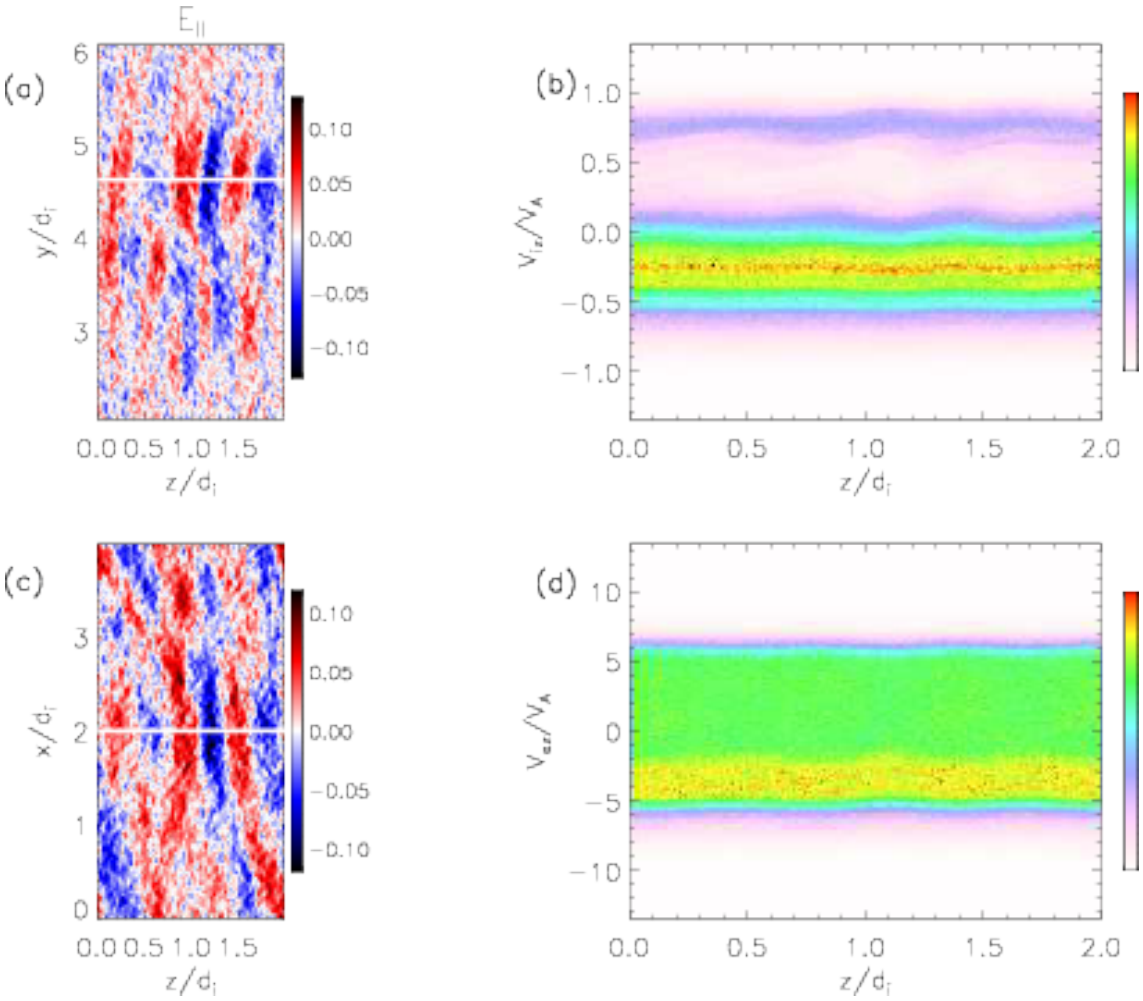

Figure 3.10: In (a) and (c) a zoom into the region around $y = 5$ of Run 4. Shown is $E_\parallel$ in y-z and x-z planes. In (b) and (d), the ion and electron phase space z-V_z along the white lines in (a) and (c).

To establish this conclusion, we use `pdrk` [7] to show that a reasonable ion distribution function can produce the basic characteristics of the instability in the simulation. Specifically, that a reasonable distribution function can lead to an elec-

trostatic instability with a maximum growth rate at the wavelength and phase speed close to that measured in the simulation. We plot this representative distribution function in Fig. 3.11(a). The two beams have velocities of -0.25 and 0.65 with thermal speeds of 0.35 and 0.13. The density ratio is 78:22. By comparing to Fig. 3.10(b), we can see that the peaks of the beams and the thermal spread of this distribution function are close to those in the simulation. We use a Maxwellian distribution of electrons with an electron temperature of 0.14 as measured in the simulation. Using `pdrk`, the growth rate, γ, is plotted versus k in the blue lines in panels (b)-(d). It produces a fastest growing mode with wave length about 0.45 and phase speed about 0.31, which is comparable to that in the simulation. So the instability is driven by the counterstreaming ions. In addition, we show the dependence of γ on mass ratio, relative drift of the two beams and the electron temperature. As in the simulations, the speed of light is chosen to be proportional to $1/\sqrt{m_e}$ so the electrons remain nonrelativistic. Panel (b) reveals that the instability is weaker with higher mass ratio, which is consistent with the simulation results. The wavelength of the fastest growing mode (normalized to the Debye length) is not sensitive to mass ratio. If we renormalize it to d_i as in the simulations, the wave length will be roughly proportional to $\sqrt{m_e}$, which is consistent with the simulations. Panels (c) and (d) show that higher relative drift or lower electron temperature have a stabilizing effect. With a small change of these parameters, the instability become stable, so the instability is close to marginal. This is consistent with the weak disturbance of the ion phase space in Fig. 3.10(b)(d). In addition, as shown in the last chapter, the relative speed of the counterstreaming ions in the exhaust is proportional to

the Alfvén speed based on the reconnecting magnetic field. Thus, if the initial β is lower (stronger magnetic field or lower temperature), the relative drift speed will be larger and the electron temperature will be lower. Therefore Figs. 3.11(c) and (d) suggest that this ion-ion instability will become stable at lower values of β. This is consistent with the discussion in Zhang et al. [73] where it was concluded that the counterstreaming ion beams would be stable in the low-β limit.

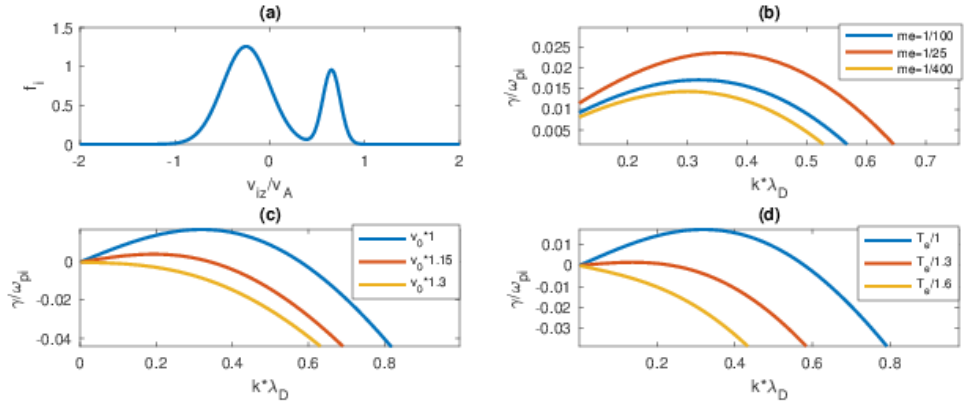

Figure 3.11: In (a) a simple model of the ion distribution prior to the ion-ion instability. The growth rates γ are plotted versus k in the blue lines in (b)-(d). The dependence of the γ on the mass ratio, the relative drift of the two beams and the electron temperature is also shown.

3.5 Conclusion

In this chapter we have used a 2D reconnection simulation, 2D and 3D Riemann simulations, and a kinetic dispersion relation solver to explore the role of instabilities and turbulence in a low-β guide field reconnection exhaust. The initial total plasma β in the simulations was chosen to be 0.1. The 2D reconnection and Riemann simulations reveal that just downstream of the x-line, the Buneman instability develops at the two RDs that bound the reconnection exhaust. The tur-

bulence in the low density RD transitions to longer wavelength and drives electron current striations that penetrate into the core of the exhaust. Further downstream the entire exhaust core exhibits large-amplitude striations that are linked to an oblique electron-beam-driven ion cyclotron instability. The electron beam driving this instability is injected from the low density RD in which the electron streaming velocity that produces the current that supports the rotation of the magnetic field points toward the core of the exhaust. However, in 3D Riemann simulations, the additional dimension strengthens the Buneman instability by allowing k_z, which is along the dominant guide field B_z, to be nonzero. This strong instability suppresses the generation of the electron beam at the low density RD with the consequence that the current striations in the core of the exhaust are largely suppressed. In addition to the Buneman instabilities at the two RD current sheets, the 3D simulation also reveals a marginal ion-ion streaming instability in the core of the exhaust. All of the instabilities that develop in the simulations become weaker with higher ion-to-electron mass ratio due to the higher electron thermal speed compared with the Alfvénic velocities associated with the dynamics of reconnection. Thus, in a system with real mass ratio, it is unclear what impact the the Buneman instability at the RDs will be. We also use the kinetic dispersion relation solver to find that this ion-ion instability will become stable with higher relative drift or lower electron temperature, which is expected under lower upstream plasma β. The direct exploration of lower β using Riemann simulations is a topic for future work.

The results suggest that in realistic low-β guide field reconnection exhausts, which exist in three dimensions and have a high ion to electron mass ratio, the

instabilities and turbulence that develop will likely be too weak to play a significant role in energy conversion. Therefore, energy conversion in the exhaust will be dominantly controlled by laminar physics with little dissipation or scattering from turbulence. The results are therefore consistent with the conclusions in the last chapter. This has broad implications for understanding reconnection in the solar corona and the inner heliosphere. The types and role of the instabilities and turbulence can be tested by the data from Parker Solar Probe [74, 75] as it approaches the low-β environment in the outer reaches of the solar corona.

Chapter 4: Conclusions

4.1 Summary

In this dissertation, we have used PIC reconnection simulations and Riemann simulations to explore the heating mechanisms and the energy partition for ions and electrons in large scale low-β reconnection exhausts with a guide field. We have also explored in depth the role of instabilities and turbulence in this energy conversion process in 2D (x-y) and 3D exhausts.

As in the MHD model, we find two RDs and two SSs developed in the exhaust. The ions are accelerated at the RDs and form counterstreaming beams downstream of the SSs, resulting in ion heating, which is proportional to the available magnetic energy per particle. The increase of the ion density from the counterstreaming beams leads to a positive potential between the SSs, which confines downstream electrons to maintain charge neutrality. The electrons are accelerated by the potential from upstream of the SS to downstream and are partly trapped by the potential in the region between the SSs, resulting in electron heating. The electron heating is limited by the amplitude of the potential. A very large potential does not develop because it would trap too many electrons compared with the modest increase in ion density and so charge neutrality would be violated. Therefore the electron heating can not

be strong even with large available magnetic energy per particle. In the low-β limit, most of the released magnetic energy goes into ion bulk flow and ion heating instead of electrons and the ion energy partition reduces to an anisotropic MHD prediction. The above mechanisms are mostly laminar because the counterstreaming ion beams are stable so that turbulence within the exhaust remains weak. The laminar SSs with little dissipation are an important difference from the MHD description.

To firmly establish the laminar nature of the reconnection exhausts, we explore the role of instabilities and turbulence in greater depth. The 2D (x-y) reconnection and Riemann simulations reveal that just downstream of the x-line, the Buneman instability develops at the two RDs. The turbulence in the low density RD transitions to longer wavelength and drives electron current striations that penetrate into the core of the exhaust. Further downstream the entire exhaust core exhibits large-amplitude striations that are linked to an oblique electron-beam-driven ion cyclotron instability. The electron beam driving this instability is injected from the low density RD. However, in 3D Riemann simulations, the additional dimension strengthens the Buneman instability by allowing large $k_{\parallel}$. This strong instability suppresses the generation of the electron beam at the low density RD and thus the current striations in the core of the exhaust. In addition to the Buneman instabilities at the two RD current sheets, the 3D simulation also reveals a marginal ion-ion streaming instability in the core of the exhaust. All of the instabilities that develop in the simulations become weaker with higher mass ratio due to the higher electron thermal speed compared with the Alfvénic velocities associated with the dynamics of reconnection. Thus, in a system with real mass ratio, it is unclear what impact

the Buneman instability at the RDs will be. We also use a kinetic dispersion relation solver to find that this ion-ion instability will become stable in conditions expected under lower upstream plasma β. The results suggest that in realistic low-β guide field reconnection exhausts, which exist in three dimensions and have a high ion to electron mass ratio, the instabilities and turbulence that develop will likely be too weak to play a significant role in energy conversion. Therefore, energy conversion in the exhaust will be dominantly controlled by the laminar physics described in the last paragraph with little dissipation or scattering from turbulence.

The result that single x-line exhausts do not produce strong electron heating or an energetic electron component suggests that the canonical solar flare picture is not enough to explain energetic electron production in large flares. Other mechanisms, such as multiple x-line reconnection, are required for electron energization.

4.2 Future Work

There are several ways to extend our studies of magnetic reconnection exhausts, using both kinetic reconnection and Riemann simulations. First, the extension of the current work into the regime of β as low as m_e/m_i would be interesting since the assumption in our analysis that the electron thermal speed is much larger than the Alfven speed is no longer valid, which might result in different electron heating scaling and stronger instabilities. Notably, there are observations suggesting that β can be this low in some coronal loop-top regions, e.g, Iwai et al. [76]

Second, it would be valuable to test our model predictions of the structures,

heating, and turbulence against observational data of reconnection exhausts in low-β environments. Such data could come from spacecrafts such as Wind and Parker Solar Probe (PSP). In particular, PSP will achieve a minimal perihelion inside 10 solar radii where the plasma parameters will be similar to those considered here. It is expected that at 10 solar radii, $B \sim 2000nT, N \sim 7000cm^{-3}, T_e \sim 85eV$ and the average β is about 0.1 [74]. Fluctuations in solar wind parameters mean that PSP should spend a significant amount of time in plasma with $\beta < 0.1$.

Finally, it would be useful to explore the "pickup ion" mechanism in reconenction exhausts far downstream of the x-line. It has been proposed that, under certain low-β conditions, ion species with sufficiently high mass-to-charge ratios will become non-adiabatic when crossing the sharp exhaust boundary [43]. These ions will be picked up by the exhaust and result in stronger ion heating. Whether the boundary of the exhaust will be as sharp further downstream and the pick up behavior persists is an open question that remains to be explored.

Appendix A: Calculation of Anisotropic MHD Solution

Since we are looking at symmetric reconnection, we only need to consider one side of the domain with one RD and one SS. According to Lin et al. [2], with pressure anisotropy, the Rankine-Hugoniot jump conditions of each discontinuity (RD or SS) are:

$$
\begin{aligned}
&[\rho V_y] = 0 \\
&\left[\rho V_y \mathbf{V_t} - \frac{B_y \mathbf{B_t}}{4\pi} + \frac{B_y \mathbf{B_t}}{8\pi}(\beta_\parallel - \beta_\perp)\right] = 0 \\
&\left[\rho V_y^2 + P_\perp + \frac{B^2}{8\pi} + \frac{B_y^2}{8\pi}(\beta_\parallel - \beta_\perp)\right] = 0 \\
&\left[\left(\frac{1}{2}\rho V^2 + \frac{5}{2}P + \frac{B^2}{4\pi} - \frac{B^2}{24\pi}(\beta_\parallel - \beta_\perp)\right) V_y - \left(1 - \frac{1}{2}(\beta_\parallel - \beta_\perp)\right) \frac{B_y \mathbf{B_t}}{4\pi} \cdot \mathbf{V_t}\right. \\
&\left. - \left(1 - \frac{1}{2}(\beta_\parallel - \beta_\perp)\right) \frac{B_y^2}{4\pi} V_y\right] = 0 \\
&[B_y \mathbf{V_t} - V_y \mathbf{B_t}] = 0
\end{aligned}
\tag{A.1}
$$

where $\rho = nm_i$, $\beta_\parallel$ and $\beta_\perp$ are plasma beta parallel and perpendicular to the local field, and $P = (P_\parallel + 2P_\perp)/3$. Subscript "t" means tangential to the shock surface.

In the low initial β limit, the perpendicular temperature (and thus pressure) throughout the solution can be neglected due to the conservation of magnetic moment. Also the parallel pressure upstream of the RD can be neglected. Similar to

Liu et al. [38], since $B_y \ll B$ and V_y is of the order of C_{Ay} in reconnection, to the lowest order the equations can be simplified to the following:

$$
\begin{aligned}
&[\rho V_y] = 0 \\
&\left[\rho V_y \mathbf{V_t} - \frac{B_y \mathbf{B_t}}{4\pi}(1 - \frac{\beta_\parallel}{2})\right] = 0 \\
&\left[\frac{B_t^2}{8\pi}\right] = 0 \\
&\left[\left(\frac{1}{2}\rho \mathbf{V_t}^2 + \frac{5}{2}3P_\parallel + \frac{B_t^2}{4\pi} - \frac{B_t^2}{24\pi}\beta_\parallel\right) V_y - \left(1 - \frac{1}{2}\beta_\parallel\right)\frac{B_y \mathbf{B_t}}{4\pi} \cdot \mathbf{V_t}\right] = 0 \\
&[B_y \mathbf{V_t} - V_y \mathbf{B_t}] = 0
\end{aligned}
\tag{A.2}
$$

There are a total of 7 jump conditions and 7 downstream unknowns here applicable to each RD or SS. The unknowns are $B_x, B_z, V_x, V_y, V_z, n, T_\parallel$. Note that the jump conditions for the RD, under the low-β assumption, will reduce to that of isotropic MHD. In addition, there are three more unknowns: the speeds in y direction in the lab frame of the SS, RD and the plasma upstream of the RD. Note that V_x and V_z upstream of the RD are zero in the lab frame. Since the reconnection is symmetric here, we also have three more constraint equations for the quantities downstream of SS, which are $B_x = 0, V_y = 0, V_z = 0$ in the lab frame. So with the same number of equations as the unknowns, we can obtain a solution for all these physical quantities.

In the solution, the speeds in y direction in the lab frame of the SS, RD and the plasma upstream of RD are $-sV_0 B_{y,u}/B_u$, $-s(C_{Ay,u} - V_0 B_{y,u}/B_u)$ and $sV_0 B_{y,u}/B_u$. Other quantities are: between the RD and SS, $B_x = 0, B_z = B_u, n = n_0, V_x = -sB_{x,u}/\sqrt{4\pi n_0 m_i}, V_z = s(B_u - B_{z,u})/\sqrt{4\pi n_0 m_i}, T_\parallel = 0, T_\perp = 0$. Between the two SSs, $B_x = 0, B_z = B_u, n = 2n_0, V_x = -sB_{x,u}/\sqrt{4\pi n_0 m_i}, V_z = 0, T_\parallel =$

$((B_u - B_{z,u})/\sqrt{4\pi n_0 m_i})^2, T_\perp = 0$.

There are a few notable features of this solution. In the lab frame there is no $\mathbf{E} \times \mathbf{B}$ flow in the y-z plane between the RD and SS as well as downstream of SS, so the field lines in the exhaust are simply stationary in the y-z plane. The speed of the slow shock, if converted to a speed along the magnetic field, is about V_0, which is the same as the inflowing speed along the fields upstream of SS. The plasma upstream of the RD has an nonzero incoming speed and the RD is traveling with upstream C_{Ay} relative to the upstream plasma.

Bibliography

[1] Masaaki Yamada, Jongsoo Yoo, Jonathan Jara-Almonte, William Daughton, Hantao Ji, Russell M Kulsrud, and Clayton E Myers. Study of energy conversion and partitioning in the magnetic reconnection layer of a laboratory plasma. *Physics of Plasmas*, 22(5):56501, may 2015.

[2] Y. Lin and L. C. Lee. Structure of reconnection layers in the magnetosphere. *Space Science Reviews*, 65(1):59–179, 1993.

[3] S K Antiochos, Z Mikić, V S Titov, R Lionello, and J A Linker. A MODEL FOR THE SOURCES OF THE SLOW SOLAR WIND. *The Astrophysical Journal*, 731(2):112, 2011.

[4] S. Tsuneta. Structure and Dynamics of Magnetic Reconnection in a Solar Flare. *The Astrophysical Journal*, 456:840, January 1996.

[5] J Egedal, W Daughton, and A Le. Large-scale electron acceleration by parallel electric fields during magnetic reconnection. *Nature Physics*, 8, 2012.

[6] J. T. Dahlin, J. F. Drake, and M. Swisdak. The mechanisms of electron heating and acceleration during magnetic reconnection. *Physics of Plasmas*, 21(9), 2014.

[7] Huasheng Xie and Yong Xiao. PDRK: A General Kinetic Dispersion Relation Solver for Magnetized Plasma. *Plasma Science and Technology*, 18(2):97–107, 2016.

[8] E.R. Priest and T.G. Forbes. The magnetic nature of solar flares. *The Astronomy and Astrophysics Review*, 10(4):313–377, Mar 2002.

[9] J Lin, W Soon, and S.L Baliunas. Theories of solar eruptions: a review. *New Astronomy Reviews*, 47(2):53 – 84, 2003.

[10] Vassilis Angelopoulos, James P. McFadden, Davin Larson, Charles W. Carlson, Stephen B. Mende, Harald Frey, Tai Phan, David G. Sibeck, Karl-Heinz Glassmeier, Uli Auster, Eric Donovan, Ian R. Mann, I. Jonathan Rae, Christopher T. Russell, Andrei Runov, Xu-Zhi Zhou, and Larry Kepko. Tail reconnection triggering substorm onset. *Science*, 321(5891):931–935, 2008.

[11] M. Yamada, F. M. Levinton, N. Pomphrey, R. Budny, J. Manickam, and Y. Nagayama. Investigation of magnetic reconnection during a sawtooth crash in a hightemperature tokamak plasma. *Physics of Plasmas*, 1(10):3269–3276, 1994.

[12] J G Doyle, J Shetye, A E Antonova, D Y Kolotkov, A K Srivastava, M Stangalini, G R Gupta, A Avramova, and M Mathioudakis. Stellar flare oscillations: evidence for oscillatory reconnection and evolution of MHD modes. *Monthly Notices of the Royal Astronomical Society*, 475(2):2842–2851, jan 2018.

[13] Elisabete M. de Gouveia Dal Pino and Alex Lazarian. Ultra–high-energy cosmic-ray acceleration by magnetic reconnection in newborn accretion-induced collapse pulsars. *The Astrophysical Journal*, 536(1):L31–L34, jun 2000.

[14] A. Lazarian and M. Opher. A MODEL OF ACCELERATION OF ANOMALOUS COSMIC RAYS BY RECONNECTION IN THE HELIOSHEATH. *The Astrophysical Journal*, 703(1):8–21, aug 2009.

[15] J. F. Drake, M. Opher, M. Swisdak, and J. N. Chamoun. A MAGNETIC RECONNECTION MECHANISM FOR THE GENERATION OF ANOMALOUS COSMIC RAYS. *The Astrophysical Journal*, 709(2):963–974, jan 2010.

[16] Y. Lyubarsky and J. G. Kirk. Reconnection in a striped pulsar wind. *The Astrophysical Journal*, 547(1):437–448, jan 2001.

[17] Pétri, J. and Lyubarsky, Y. Magnetic reconnection at the termination shock in a striped pulsar wind. *A&A*, 473(3):683–700, 2007.

[18] Kris Beckwith, John F. Hawley, and Julian H. Krolik. The influence of magnetic field geometry on the evolution of black hole accretion flows: Similar disks, drastically different jets. *The Astrophysical Journal*, 678(2):1180–1199, may 2008.

[19] E. N. Parker. Sweet's mechanism for merging magnetic fields in conducting fluids. *Journal of Geophysical Research (1896-1977)*, 62(4):509–520.

[20] P. A. Sweet. 14. the neutral point theory of solar flares. *Symposium - International Astronomical Union*, 6:123134, 1958.

[21] H. E. Petschek. *Magnetic Field Annihilation*, volume 50, page 425. 1964.

[22] D A Uzdensky and R M Kulsrud. Two-dimensional numerical simulation of the resistive reconnection layer. *Physics of Plasmas*, 7(10):4018–4030, sep 2000.

[23] Masayuki Ugai and Takao Tsuda. Magnetic field-line reconnexion by localized enhancement of resistivity: Part 1. evolution in a compressible mhd fluid. *Journal of Plasma Physics*, 17(3):337356, 1977.

[24] J.D. Huba, N.T. Gladd, and K. Papadopoulos. The lower-hybrid-drift instability as a source of anomalous resistivity for magnetic field line reconnection. *Geophys. Res. Lett.; (United States)*.

[25] J. F. Drake, M. Swisdak, C. Cattell, M. A. Shay, B. N. Rogers, and A. Zeiler. Formation of electron holes and particle energization during magnetic reconnection. *Science*, 299(5608):873–877, 2003.

[26] H. Che, J. F. Drake, M. Swisdak, and P. H. Yoon. Electron holes and heating in the reconnection dissipation region. *Geophysical Research Letters*, 37(11).

[27] Y.-M. Wang, N R Sheeley Jr., D G Socker, R A Howard, and N B Rich. The dynamical nature of coronal streamers. *Journal of Geophysical Research: Space Physics*, 105(A11):25133–25142, nov 2000.

[28] Vyacheslav S Titov, Gunnar Hornig, and Pascal Démoulin. Theory of magnetic connectivity in the solar corona. *Journal of Geophysical Research: Space Physics*, 107(A8):SSH 3–1–SSH 3–13, aug 2002.

[29] V S Titov. Generalized Squashing Factors for Covariant Description of Magnetic Connectivity in the Solar Corona. *The Astrophysical Journal*, 660(1):863–873, 2007.

[30] E. N. Parker. Nanoflares and the Solar X-Ray Corona. , 330:474, Jul 1988.

[31] M Oka, S Ishikawa, P Saint-Hilaire, S Krucker, and R P Lin. KAPPA DISTRIBUTION MODEL FOR HARD X-RAY CORONAL SOURCES OF SOLAR FLARES. *The Astrophysical Journal*, 764(1):6, 2013.

[32] Mitsuo Oka, Sm Krucker, Hugh S. Hudson, and Pascal Saint-Hilaire. Electron energy partition in the above-the-looptop solar hard x-ray sources. *The Astrophysical Journal*, 799(2):129, 2015.

[33] R. P. Lin, S. Krucker, G. J. Hurford, D. M. Smith, H. S. Hudson, G. D. Holman, R. A. Schwartz, B. R. Dennis, G. H. Share, R. J. Murphy, A. G. Emslie, C. Johns-Krull, and N. Vilmer. Rhessi observations of particle acceleration and energy release in an intense solar gamma-ray line flare. *The Astrophysical Journal Letters*, 595(2):L69, 2003.

[34] S. E. Guidoni and D. W. Longcope. Shocks and thermal conduction fronts in retracting reconnected flux tubes. *The Astrophysical Journal*, 718(2):1476, 2010.

[35] S. E. Guidoni and D. W. Longcope. Density enhancements and voids following patchy reconnection. *The Astrophysical Journal*, 730(2):90, 2011.

[36] J. F. Drake, M. Swisdak, C. Cattell, M. A. Shay, B. N. Rogers, and A. Zeiler. Formation of electron holes and particle energization during magnetic reconnection. *Science*, 299(5608):873–877, 2003.

[37] P. L. Pritchett and F. V. Coroniti. Three-dimensional collisionless magnetic reconnection in the presence of a guide field. *Journal of Geophysical Research: Space Physics*, 109(A1), 2004. A01220.

[38] Yi-Hsin Liu, J. F. Drake, and M. Swisdak. The structure of the magnetic reconnection exhaust boundary. *Physics of Plasmas*, 19(2), 2012.

[39] M. A. Shay, C. C. Haggerty, T. D. Phan, J. F. Drake, P. A. Cassak, P. Wu, M. Øieroset, M. Swisdak, and K. Malakit. Electron heating during magnetic reconnection: A simulation scaling study. *Physics of Plasmas*, 21(12), 2014.

[40] C. C. Haggerty, M. A. Shay, J. F. Drake, T. D. Phan, and C. T. McHugh. The competition of electron and ion heating during magnetic reconnection. *Geophysical Research Letters*, 42(22):9657–9665, 2015. 2015GL065961.

[41] J. Egedal, W. Daughton, A. Le, and A. L. Borg. Double layer electric fields aiding the production of energetic flat-top distributions and superthermal electrons within magnetic reconnection exhausts. *Physics of Plasmas*, 22(10), 2015.

[42] J. F. Drake, M. Swisdak, T. D. Phan, P. A. Cassak, M. A. Shay, S. T. Lepri, R. P. Lin, E. Quataert, and T. H. Zurbuchen. Ion heating resulting from pickup in magnetic reconnection exhausts. *Journal of Geophysical Research: Space Physics*, 114(5), may 2009.

[43] J. F. Drake, P. A. Cassak, M. A. Shay, M. Swisdak, and E. Quataert. a Magnetic Reconnection Mechanism for Ion Acceleration and Abundance Enhancements in Impulsive Flares. *The Astrophysical Journal*, 700(1):L16–L20, 2009.

[44] W. Daughton, V. Roytershteyn, H. Karimabadi, L. Yin, B. J. Albright, B. Bergen, and K. J. Bowers. Role of electron physics in the development of turbulent magnetic reconnection in collisionless plasmas. *Nature Physics*, 7:539–542, July 2011.

[45] J. T. Dahlin, J. F. Drake, and M. Swisdak. Electron acceleration in three-dimensional magnetic reconnection with a guide field. *Physics of Plasmas*, 22(10), 2015.

[46] T. D. Phan, M. A. Shay, J. T. Gosling, M. Fujimoto, J. F. Drake, G. Paschmann, M. Øieroset, J. P. Eastwood, and V. Angelopoulos. Electron bulk heating in magnetic reconnection at earth's magnetopause: Dependence on the inflow alfvn speed and magnetic shear. *Geophysical Research Letters*, 40(17):4475–4480, 2013.

[47] T. D. Phan, J. F. Drake, M. A. Shay, J. T. Gosling, G. Paschmann, J. P. Eastwood, M. Øieroset, M. Fujimoto, and V. Angelopoulos. Ion bulk heating in magnetic reconnection exhausts at earth's magnetopause: Dependence on the inflow alfvn speed and magnetic shear angle. *Geophysical Research Letters*, 41(20):7002–7010, 2014. 2014GL061547.

[48] A. Zeiler, D. Biskamp, J. F. Drake, B. N. Rogers, M. A. Shay, and M. Scholer. Threedimensional particle simulations of collisionless magnetic reconnection. *Journal of Geophysical Research: Space Physics (19782012)*, 107(A9):SMP 6–1–SMP 6–9, 9 2002.

[49] Y. Lin and D. W. Swift. A two-dimensional hybrid simulation of the magnetotail reconnection layer. *Journal of Geophysical Research: Space Physics*, 101(A9):19859–19870, 1996.

[50] M. Scholer and R.-F. Lottermoser. On the kinetic structure of the magnetotail reconnection layer. *Geophysical Research Letters*, 25(17):3281–3284, 1998.

[51] Michael Cremer and Manfred Scholer. Collisionless slow shocks in magnetotail reconnection. *Geophysical Research Letters*, 26(17):2709–2712, 1999.

[52] Michael Cremer and Manfred Scholer. Structure of the reconnection layer and the associated slow shocks: Two-dimensional simulations of a riemann problem. *Journal of Geophysical Research: Space Physics*, 105(A12):27621–27632, 2000.

[53] Yi-Hsin Liu, J. F. Drake, and M. Swisdak. The effects of strong temperature anisotropy on the kinetic structure of collisionless slow shocks and reconnection exhausts. i. particle-in-cell simulations. *Physics of Plasmas*, 18(6), 2011.

[54] Yi-Hsin Liu, J. F. Drake, and M. Swisdak. The effects of strong temperature anisotropy on the kinetic structure of collisionless slow shocks and reconnection exhausts. ii. theory. *Physics of Plasmas*, 18(9), 2011.

[55] William E Drummond and Marshall N Rosenbluth. Anomalous Diffusion Arising from Microinstabilities in a Plasma. *The Physics of Fluids*, 5(12):1507–1513, dec 1962.

[56] N. A. Krall and A. W. Trivelpiece. *Principles of plasma physics*. McGraw-Hill, 1973.

[57] TAKAO Fujita, TOSHIRO Ohnuma, and SABURO Adach. Self-oscillations excited by two stream ion-ion instability. *Plasma Phys.*, 19:875–887, 1977.

[58] Michael E. Rowan, Lorenzo Sironi, and Ramesh Narayan. Electron and proton heating in transrelativistic guide field reconnection. *The Astrophysical Journal*, 873(1):2, feb 2019.

[59] D W Longcope and S J Bradshaw. SLOW SHOCKS AND CONDUCTION FRONTS FROM PETSCHEK RECONNECTION OF SKEWED MAGNETIC FIELDS: TWO-FLUID EFFECTS. *The Astrophysical Journal*, 718(2):1491–1508, 2010.

[60] J F Drake, M Swisdak, H Che, and M A Shay. Electron acceleration from contracting magnetic islands during reconnection. *Nature*, 443(7111):553–556, 2006.

[61] J. F. Drake, M. Swisdak, and R. Fermo. The power-law spectra of energetic particles during multi-island magnetic reconnection. *The Astrophysical Journal Letters*, 763(1):L5, 2013.

[62] J T Dahlin, J F Drake, and M Swisdak. The role of three-dimensional transport in driving enhanced electron acceleration during magnetic reconnection. *Physics of Plasmas*, 24(9):92110, sep 2017.

[63] C Cattell, J Dombeck, J Wygant, J F Drake, M Swisdak, M L Goldstein, W Keith, A Fazakerley, M André, E Lucek, and A Balogh. Cluster observations of electron holes in association with magnetotail reconnection and comparison to simulations. *Journal of Geophysical Research: Space Physics*, 110(A1), jan 2005.

[64] H Che, J F Drake, and M Swisdak. A current filamentation mechanism for breaking magnetic field lines during reconnection. *Nature*, 474:184, jun 2011.

[65] D B Graham, Yu. V Khotyaintsev, C Norgren, A Vaivads, M André, S Toledo-Redondo, P.-A. Lindqvist, G T Marklund, R E Ergun, W R Paterson, D J Gershman, B L Giles, C J Pollock, J C Dorelli, L A Avanov, B Lavraud, Y Saito, W Magnes, C T Russell, R J Strangeway, R B Torbert, and J L Burch. Lower hybrid waves in the ion diffusion and magnetospheric inflow regions. *Journal of Geophysical Research: Space Physics*, 122(1):517–533, jan 2017.

[66] L Price, M Swisdak, J F Drake, P A Cassak, J T Dahlin, and R E Ergun. The effects of turbulence on three-dimensional magnetic reconnection at the magnetopause. *Geophysical Research Letters*, 43(12):6020–6027, jun 2016.

[67] A Le, W Daughton, L.-J. Chen, and J Egedal. Enhanced electron mixing and heating in 3-D asymmetric reconnection at the Earth's magnetopause. *Geophysical Research Letters*, 44(5):2096–2104, mar 2017.

[68] L Price, M Swisdak, J F Drake, J L Burch, P A Cassak, and R E Ergun. Turbulence in Three-Dimensional Simulations of Magnetopause Reconnection. *Journal of Geophysical Research: Space Physics*, 122(11):11,11–86,99, nov 2017.

[69] P A Muñoz and J Büchner. Non-Maxwellian electron distribution functions due to self-generated turbulence in collisionless guide-field reconnection. *Physics of Plasmas*, 23(10):102103, oct 2016.

[70] F Pucci, S Servidio, L Sorriso-Valvo, V Olshevsky, W H Matthaeus, F Malara, M V Goldman, D L Newman, and G Lapenta. Properties of Turbulence in the Reconnection Exhaust: Numerical Simulations Compared with Observations. *The Astrophysical Journal*, 841(1):60, 2017.

[71] J P Eastwood, R Mistry, T D Phan, S J Schwartz, R E Ergun, J F Drake, M Øieroset, J E Stawarz, M V Goldman, C Haggerty, M A Shay, J L Burch, D J Gershman, B L Giles, P A Lindqvist, R B Torbert, R J Strangeway, and C T Russell. Guide Field Reconnection: Exhaust Structure and Heating. *Geophysical Research Letters*, 45(10):4569–4577, may 2018.

[72] He Jiansen, Zhu Xingyu, Chen Yajie, Salem Chadi, Stevens Michael, Li Hui, Ruan Wenzhi, Zhang Lei, and Tu Chuanyi. Plasma Heating and Alfvénic Turbulence Enhancement During Two Steps of Energy Conversion in Magnetic Reconnection Exhaust Region of Solar Wind. *The Astrophysical Journal*, 856(2):148, 2018.

[73] Qile Zhang, J. F. Drake, and M. Swisdak. Particle heating and energy partition in low-β guide field reconnection with kinetic riemann simulations. *Physics of Plasmas*, 2019, accepted.

[74] S D Bale, K Goetz, P R Harvey, P Turin, J W Bonnell, T Dudok de Wit, R E Ergun, R J MacDowall, M Pulupa, M Andre, M Bolton, J.-L. Bougeret, T A Bowen, D Burgess, C A Cattell, B D G Chandran, C C Chaston, C H K Chen, M K Choi, J E Connerney, S Cranmer, M Diaz-Aguado, W Donakowski, J F Drake, W M Farrell, P Fergeau, J Fermin, J Fischer, N Fox, D Glaser, M Goldstein, D Gordon, E Hanson, S E Harris, L M Hayes, J J Hinze, J V Hollweg, T S Horbury, R A Howard, V Hoxie, G Jannet, M Karlsson, J C Kasper, P J Kellogg, M Kien, J A Klimchuk, V V Krasnoselskikh, S Krucker, J J Lynch, M Maksimovic, D M Malaspina, S Marker, P Martin, J Martinez-Oliveros, J McCauley, D J McComas, T McDonald, N Meyer-Vernet, M Moncuquet, S J Monson, F S Mozer, S D Murphy, J Odom, R Oliverson, J Olson, E N Parker, D Pankow, T Phan, E Quataert, T Quinn, S W Ruplin, C Salem, D Seitz, D A Sheppard, A Siy, K Stevens, D Summers, A Szabo, M Timofeeva, A Vaivads, M Velli, A Yehle, D Werthimer, and J R Wygant. The FIELDS Instrument Suite for Solar Probe Plus. *Space Science Reviews*, 204(1):49–82, 2016.

[75] Justin C Kasper, Robert Abiad, Gerry Austin, Marianne Balat-Pichelin, Stuart D Bale, John W Belcher, Peter Berg, Henry Bergner, Matthieu Berthomier, Jay Bookbinder, Etienne Brodu, David Caldwell, Anthony W Case, Benjamin D G Chandran, Peter Cheimets, Jonathan W Cirtain, Steven R Cranmer, David W Curtis, Peter Daigneau, Greg Dalton, Brahmananda Dasgupta, David DeTomaso, Millan Diaz-Aguado, Blagoje Djordjevic, Bill Donaskowski, Michael Effinger, Vladimir Florinski, Nichola Fox, Mark Freeman, Dennis Gallagher, S Peter Gary, Tom Gauron, Richard Gates, Melvin Goldstein, Leon Golub, Dorothy A Gordon, Reid Gurnee, Giora Guth, Jasper Halekas, Ken Hatch, Jacob Heerikuisen, George Ho, Qiang Hu, Greg Johnson, Steven P Jordan, Kelly E

Korreck, Davin Larson, Alan J Lazarus, Gang Li, Roberto Livi, Michael Ludlam, Milan Maksimovic, James P McFadden, William Marchant, Bennet A Maruca, David J McComas, Luciana Messina, Tony Mercer, Sang Park, Andrew M Peddie, Nikolai Pogorelov, Matthew J Reinhart, John D Richardson, Miles Robinson, Irene Rosen, Ruth M Skoug, Amanda Slagle, John T Steinberg, Michael L Stevens, Adam Szabo, Ellen R Taylor, Chris Tiu, Paul Turin, Marco Velli, Gary Webb, Phyllis Whittlesey, Ken Wright, S T Wu, and Gary Zank. Solar Wind Electrons Alphas and Protons (SWEAP) Investigation: Design of the Solar Wind and Coronal Plasma Instrument Suite for Solar Probe Plus. *Space Science Reviews*, 204(1):131–186, 2016.

[76] Kazumasa Iwai, Kiyoto Shibasaki, Satoshi Nozawa, Takuya Takahashi, Shinpei Sawada, Jun Kitagawa, Shun Miyawaki, and Hirotaka Kashiwagi. Coronal magnetic field and the plasma beta determined from radio and multiple satellite observations. *Earth, Planets and Space*, 66(1):149, 2014.